Title

Effective mechanical potential of cell–cell interaction explains basic structures of three-dimensional morphogenesis

Short title

Effective potential of cell–cell interaction on morphogenesis

Authors

Hiroshi Koyama[1,2,*], Hisashi Okumura[2,3,4], Atsushi M. Ito[5], Tetsuhisa Otani[2,6], Kazuyuki Nakamura[7,8], Kagayaki Kato[2,9,10], and Toshihiko Fujimori[1,2]

[1]Division of Embryology, National Institute for Basic Biology, 5-1 Higashiyama, Myodaiji, Okazaki, Aichi 444-8787, Japan

[2]SOKENDAI (The Graduate University for Advanced Studies), Hayama, Kanagawa 240-0193, Japan

[3]Biomolecular Dynamics Simulation Group, Exploratory Research Center on Life and Living Systems (ExCELLS), National Institutes of Natural Sciences, 5-1 Higashiyama, Myodaiji, Okazaki, Aichi 444-8787, Japan

[4]Institute for Molecular Science, National Institutes of Natural Sciences, 5-1 Higashiyama, Myodaiji, Okazaki, Aichi 444-8787, Japan

[5]Department of Helical Plasma Research, National Institute for Fusion Science, National Institutes of Natural Sciences, 322-6 Oroshi-cho, Toki, Gifu 509-5292, Japan

[6]Division of Cell Structure, National Institute for Physiological Sciences, 5-1 Higashiyama, Myodaiji, Okazaki, Aichi 444-8787, Japan

[7]School of Interdisciplinary Mathematical Sciences, Meiji University, 4-21-1 Nakano, Nakano-ku, Tokyo 164-8525, Japan

[8]JST, PRESTO, 4-1-8 Honcho, Kawaguchi, Saitama 332-0012, Japan

[9]Bioimage Informatics Group, Exploratory Research Center on Life and Living Systems (ExCELLS), National Institutes of Natural Sciences, 38 Nishigonaka, Myodaiji, Okazaki, Aichi 444-8585, Japan

[10]Laboratory of biological diversity, National Institute for Basic Biology, 38 Nishigonaka, Myodaiji, Okazaki, Aichi 444-8585, Japan

*Correspondence: Hiroshi Koyama

Division of Embryology, National Institute for Basic Biology, 5-1 Higashiyama, Myodaiji, Okazaki, Aichi 444-8787, Japan

Phone: +81 564 59 5862,

hkoyama@nibb.ac.jp.

Keywords

effective potential of cell–cell interaction, morphological diversity, mechanics, multi-cellular system, coarse-grained model

Abstract

Mechanical properties of cell–cell interactions have been suggested to be critical for the emergence of diverse three-dimensional morphologies of multicellular organisms. Mechanical potential energy of cell–cell interactions has been theoretically assumed, however, whether such potential can be detectable in living systems remains poorly understood. In this study, we developed a novel framework for inferring mechanical forces of cell–cell interactions. First, by analogy to coarse-grained models in molecular and colloidal sciences, cells were approximately assumed to be spherical particles, where microscopic features of cells such as polarities and shapes were not explicitly incorporated and the mean forces (i.e. effective forces) of cell–cell interactions were considered. Then, the forces were statistically inferred from live imaging data, and subsequently, we successfully detected potentials of cell–cell interactions. Finally, computational simulations based on these potentials were performed to test whether these potentials can reproduce the original morphologies. Our results from various systems, including Madin-Darby canine kidney (MDCK) cells, *C.elegans* early embryos, and mouse blastocysts, suggest that the method can accurately infer the effective potentials and capture the diverse three-dimensional morphologies. Importantly, energy barriers were predicted to exist at the distant regions of the interactions, and this mechanical

property of cell–cell interactions was essential for formation of cavities, tubes, cups, and two-dimensional sheets. Collectively, these structures constitute basic structures observed during morphogenesis and organogenesis. We propose that effective potentials of cell–cell interactions are parameters that can be measured from living organisms, and represent a fundamental principle underlying the emergence of diverse three-dimensional morphogenesis.

Introduction

The mechanical properties of interactions between objects are among the most fundamental parameters of various physical, chemical, and biological phenomena at a wide range of spatial scales in the molecular, colloidal, cellular, and astrophysical sciences. Interactions among particulate matter such as ions, molecules, and colloids are primarily mediated by electromagnetic forces, and the properties of these interactions, including attractive and repulsive forces, substantially affect the dynamics and stability of systems [1,2]. In multi-cellular living systems, various three-dimensional morphologies are observed. The emergence of these diverse morphologies is thought to be primarily dependent on the mechanical properties of the constituent cells. In particular, mechanical properties of cell–cell interactions are involved in morphogenetic events such as epithelial cell movement and cell sorting [3–7]. However, the mechanical basis of morphogenesis, which gives rise to a variety of structures, remains to be elucidated, and it is not yet known whether any unifying principle can explain the morphological diversity of organs and tissues.

The mechanical properties of cell–cell interactions are regulated by various factors. In epithelial cells, whose shapes are typically columnar polygons, cell–cell adhesion energy is controlled by cadherin family proteins (Fig. S1A-i and B) [3,4,8], whereas

actomyosin proteins counteract adhesion through the indirect effect of cell surface tension (Fig. S1A-i and B) [9,10]. Moreover, cellular polarities such as apico-basal polarity are linked to biased localization of cadherin proteins, leading to directional differences in properties of cell–cell interactions. By contrast, in mesenchymal cells, which are unstructured shapes, in addition to cadherins, cell–cell interactions are regulated by indirect interactions through extracellular matrix (i.e. substrate) (Fig.S1A-i) [11–13]. Therefore, cell–cell interactions entail many microscopic parameters determined by various proteins and cellular processes, resulting in very complex physics with many degrees of freedom (Fig.S1A-i). To elucidate the principles underlying morphological diversity, it is essential to investigate how the integrated effects of many microscopic parameters can be described as simple meso or macroscopic parameters (Fig. S1A-ii).

In non-living materials such as ions, molecules, and colloids, interactions among particulate matter are determined by electron clouds (i.e. quantum state), which have complex shapes (Fig. S1A-iii) [14]. On the other hand, mechanical potential energies of particle–particle interactions have been successfully described as a function of distances of the interactions, e.g. the Lenard–Jones potential which is usually applied to rare gas atoms (Fig. S1A-iv). Therefore, it can be interpreted that the microscopic components conferred from electron clouds can be integrated into the potentials of particle–particle

interactions as mesoscopic parameters. Typically, such distance–potential curve contains repulsive forces around regions of short distances, which are provided from excluded volume effect of the particles, and attractive forces around regions of middle and far distances (Fig. 1B, and Fig. appx 1). Intriguingly, in the case of non-spherical or polarized molecules including water and amino acids, potentials of their interactions have been sometimes defined as a function of distances where the molecules are assumed as isotropic particles. These coarse-grained models have been succeeded to explain overall behaviors of the systems with a trade-off of microscopic accuracy [14].

In atomic and molecular sciences, how various microscopic components are integrated into potentials of particle–particle interactions have been theoretically established well in relatively simple systems [2,14], which we call here a bottom-up approach. On the other hand, there are top-down approaches to obtain the potentials. Potential energies of whole systems according to atomic or molecular configurations are calculated from simulations on the basis of quantum chemistry which is more accurate than classical mechanics. Then, by using the calculated potential energies and the configurations as reference data, potentials of particle–particle interactions have been inferred through trial-and-errors searches or machine learning [1,2,15]. The simplest example is a usage of radial distribution functions as reference data, because the functions mean

125 probability of particle positions along particle–particle distances, which can be linked to
126 potential energy (Fig. appx 1 and SI, Appendix section 12-1) [2]. Because these potentials
127 are the outcomes from various microscopic components, they are "effective" potentials
128 of particle–particle interactions. Using these potentials obtained from the bottom-up or
129 top-down approaches as an integrative parameter, many molecular dynamics simulations
130 have been successfully performed to understand the dynamics and shapes of various
131 systems (Fig. S1) [16].

132 The potential of cell–cell interaction is also conceptually well recognized, and
133 has been used in theoretical studies (Fig. 1B and S1A-ii) [11,17–25]. The potential energy can
134 be defined regardless of whether two cells directly contact each other. Although adhesive
135 forces between two isolated cells have been measured (i.e. forces required to dissociate
136 one cell from the other) [6,26], they have neither been measured nor inferred in more
137 complex multi-cellular systems, which differ from isolated cells. For instance, cell shapes
138 in multi-cellular systems are entirely different from those of isolated cells: they can be far
139 from spherical shapes (e.g. flattened shape). Apico-basal polarity cannot be defined in
140 isolated cells but can be in cell sheets whose three-dimensional directions are determined
141 by extracellular matrix (ECM) or substrate (Fig. 1 and S1). If effective potentials of cell–
142 cell interactions could be defined as a parameter integrating these various factors, the

effective potentials would be useful to explain shapes and dynamics of multi-cellular systems. However, it is challenging to identify all these factors and measure the values of their related-parameters, which is a bottleneck to obtain effective potentials through bottom-up approaches.

In this study, by analogy to non-living materials (Fig. 1), we tried a top-down approach: we developed a method for statistically inferring the effective potential of cell–cell interactions using nuclear tracking data from live imaging as reference data, which are relatively easy to obtain. Thus, shapes and polarities of cells were not explicitly considered at this moment, whose effects we tried to decode after acquiring inference results (Fig. 1I). Our method was validated by using various artificially-generated data with or without external factors such as egg shells, cavities, and traction forces exerted between cells and substrates. Then, we tested whether effective potentials of cell–cell interactions are detected in living systems. We applied this method to relatively small multi-cellular systems (4–350 cells) including mouse pre-implantation embryos bearing cavities and early embryos of the nematode *Caenorhabditis elegans* bearing egg shells. We clearly detected effective potentials as a function of cell–cell distances in these systems. Further theoretical analyses suggested that effective potential represents a unifying principle capable of explaining various structures including cell aggregates,

cavities, tubes, cups (round and hollow shapes), and two-dimensional sheets (Fig. 1H). Because these structures are formed prior to the morphogenesis of complex tissue structures, we consider these as basic structural units during three-dimensional morphogenesis. We also describe the differences in these potentials between living and non-living materials, as well as among biological species.

Theory and principle for inferring effective potential

Overview of strategy for inferring effective potentials/forces of cell–cell interaction

To measure or infer the effective potentials or forces of cell–cell interactions *in vivo*, we developed a particle-based cell model in which attractive or repulsive forces are exerted between each pair of cells (Fig. 1A, B and D). This coarse-grained model does not explicitly incorporate microscopic features of cells such as cell shape, polarities, size, heterogeneity, cell type or origin (e.g., epithelial, mesenchymal, or blastomere cells), etc. at this moment (Fig. 1C, D and S1A). Simultaneously, we obtained time series of three-dimensional cell positions from confocal microscopic images (Fig. 1E) and statistically inferred the forces of cell–cell interactions by systematically searching for force values that could reproduce the cell movements observed *in vivo* (Fig. 1F). Since the inferred forces are the outcome from the integrative effects of the microscopic features of cells, we call the forces "effective forces". To validate the method, we utilized artificial cell movement data generated by performing simulations under given potentials of cell–cell interactions, and confirmed that the inferred forces were consistent with the given-potentials. The details of each part of the analysis are explained in the following sections.

Particle-based cell models

185 In our model, particles interact with each other and attractive or repulsive forces

186 (F_i) are assumed (Fig. 1D), where i is an identifier for particle–particle interactions. In

187 three-dimensional cellular systems with no attachment to substrates, we did not assume

188 persistent random walks which are originated from cellular traction forces on substrates

189 [27,28].

190 The equation of particle motions is defined below. In cellular-level phenomena,

191 viscous drag force or frictional force provided by the surrounding medium or tissue is

192 dominant, as expected from the low Reynolds number; consequently, the inertial force is

193 negligible in general [5,11,13,29,30]. The forces in such a system can be assumed to be

194 correlated with the velocities of the objects [5,13,24,25,31]. Thus, the velocity (V_p) of a particle

195 is calculated by the net force (F_p) exerted on the particle as follows:

196 $$V_p = F_p / \gamma \qquad \text{(Eq. 1)},$$

197 where p is an identifier for particles and γ is the coefficient of viscous drag and frictional

198 forces. F_p is the summation of F_i: $F_p = \sum_{i=1}^{I} \delta(p) F_i$, where I is the total number of

199 interactions, and in the case that the ith interaction is formed with the pth particle, $\delta(p)$ is

200 1, otherwise $\delta(p)$ is 0 (Fig. 1D). We assumed the simplest situation, i.e., γ is constant

201 (=1.0). Thus, by giving the values of F_i from, for instance, a distance–potential curve, a

202 simulation can run. The influence of these assumptions on simulation results is discussed

203 in SI (Section 4-4, 4-6-2, and 7).

204

205 *Data acquisition of time series of cell positions*

206 To define cell positions, we focused on nuclei, because they are most easily
207 imaged by microscopy (Fig. 1E). In fact, nuclear detection followed by temporal tracking
208 has been performed in a wide range of organisms from *C. elegans* to mammals, and these
209 data are accumulating [32–36]. We utilized publicly available nuclear tracking data of a
210 developing embryo of *C. elegans* [32]; nuclear tracking data of developing mouse embryos
211 and MDCK cultured cells were obtained in this study (SI, Section 2, 8, and 11 with text
212 data). Procedures for tracking cell division are described in SI (Section 3) and Figure S2B.

213

214 *Development of method for inferring effective potentials/forces of cell-cell interaction*

215 In the case of ions, molecules, etc., radial distribution functions are often
216 measured and used to infer the effective potentials of their interactions (Fig. appx 1 and
217 SI, Appendix section 12-1) [1,2]. Although this method is simple and applicable to
218 thermodynamically equilibrium systems, it is not suitable for non-equilibrium systems,
219 including morphogenetic events. To infer the effective potentials of non-equilibrium
220 systems, we fitted the particle-based cell model to the time series of nuclear positions in

221 the spirit of data assimilation, where the fitting parameters are forces between all pairs of
222 cell–cell interactions (the total number is I, as previously defined) for each time frame.
223 Data assimilation is a technique to solve an inverse problem for a simulation-based model
224 [37,38]. One of well-known model fittings is based on least squares in combination with a
225 linear model (function-based model), resulting in inference of parameter values of the
226 linear function. In data assimilation, models to be fitted are simulation-based models
227 instead of function-based models, whereas least squares are also often used to infer
228 parameter values which are usually numerically solved (Fig. appx 3 and SI, Appendix
229 section 12-3). Through repeated cycles of simulations of the model, we systematically
230 searched for the values of the effective forces between all pairs of cell–cell interactions
231 that minimized the differences (i.e. corresponding to least squares) between the particle
232 positions in the simulations and the *in vivo* nuclear positions (Fig. 1, and S2C). The
233 differences (G_{xyz}) to be minimized are defined as follows (SI, Section 4-1 and 4-2).

234 $$G_{xyz} = \sum_{t=1}^{T} \sum_{p=1}^{P(t)} \frac{\left\{x_p(t) - x_p^{\mathrm{ref}}(t)\right\}^2 + \left\{y_p(t) - y_p^{\mathrm{ref}}(t)\right\}^2 + \left\{z_p(t) - z_p^{\mathrm{ref}}(t)\right\}^2}{\Delta t}$$

235 (Eq. 2)

236 Here, p is an identifier for particles, t is an identifier for time frames, and Δt is
237 the time interval between the time frames. The x, y, and z coordinates of the pth particle
238 obtained from microscopic images are x_p^{ref}, y_p^{ref}, and z_p^{ref}; ref means reference (Fig. S2C).

The coordinates during the repeated cycles of simulations are x_p, y_p, and z_p. The effective forces were inferred for each cell–cell pair for each time frame (Fig. S2B and C). Note that, because γ was assumed to be constant in Equation 1, we can only infer relative but not absolute values of effective forces. To determine whether our method can correctly infer effective forces, we first applied it to artificial data generated under given potentials of particle–particle interactions, and examined whether the inferred effective forces were consistent with the given potentials (Fig. S3A). We tried the Lenard–Jones (LJ) potential as a test case of the given potentials, which is originated from atom–atom interactions but is one of the most well-known potentials used in various fields including biology [39]. By performing particle simulations under the LJ potentials, we obtained time series of the particle positions (Fig. S3A, SI, Section 4-3-4-1, and Movie S1A). Then, we applied the inference method to the time series, yielding effective forces for each pair of particles for each time frame (Fig. S3B). The inferred effective forces were plotted against particle–particle distance (Fig. S2D, S3C, and SI, Section 5). By averaging the plots for each shallow bin of distances, we obtained distance–force (DF) curves (Fig. S3C). We found that the DF curves were not consistent with the curve from the LJ potentials, suggesting that Equation 2 was not optimal. Therefore, we tried to incorporate various additional constraints (i.e. cost functions during the minimization procedures) into Equation 2. We

257 found that, when a cost function was set so that force values approach zero at long distant
258 regions of cell–cell interactions (SI, Section 4-3, Equation S6), inferred DF curves
259 became consistent with that from the LJ potentials (Fig. S3). Detailed principles, rational,
260 and procedures are described in SI (Section 4). Additionally, if this cost function was not
261 incorporated, this minimization problem exhibited indefiniteness (i.e., a unique solution
262 could not be determined) and over-fitting also occurred (Fig. appx 3). This cost function
263 is considered as the prior in the Bayesian inference, and, in general, a unique solution
264 could be ensured by introducing such a prior [37].

265 Using Equation S6 containing the above cost function (SI, Section 4-3), we also
266 tried other potentials generated by freehand drawing, called "FH" potentials in this study,
267 as an alternative to the LJ potentials (Fig. S3A and Movie S1B). The FH potentials were
268 chosen because the simulation outcomes under the FH potentials differ from those under
269 the LJ potentials as shown later (Fig. S11). The inferred DF curves were almost consistent
270 with the given potentials (Fig. S3C, E, and SI, Section 4-3-4). Conversely, we also tried
271 using time series of random–walk simulations as negative controls (Fig. S3A and Movie
272 S1C). The plots of the inferred effective forces against distances were widely distributed,
273 and the DF curves generated from the plots by averaging were zigzag and disorganized
274 (Fig. S3C and E). These results indicate that our method can correctly infer DF curves.

Results

Systematic validation of inference method using artificial data

We first systematically validated our inference method using artificial data which include various external factors. Specifically, we assessed whether spatial constraints such as egg shells or cavities can affect inference results of effective forces of cell–cell interactions. Similar to the previous section, "Theory and principle for inferring effective potential", we generated artificial data based on simulations under LJ potential, to which we applied our inference method.

In the absence of spatial constraints, inferred distance–force (DF) curves were well consistent with the DF curves derived from the LJ potential under various settings of simulations: the settings are related to time interval of sampling, cell proliferation, and fluctuation of forces between cell–cell interactions (Fig. 2A-B, S4-I, -II, -III, SI, Section 4-4, 7-4, and Movie S8A-E). Next, we introduced spatial constraints corresponding to eggshells (SI, section 7-4-2 and Movie S8F-I). Even under narrow cylindrical constraints, inferred DF curves were well consistent with the DF curves from the LJ potential (Fig. 2C; length of cylinder = 25μm, S4-V, and SI, Section 4-4). By contrast, under constraints

293 with smaller volume where each particle was highly compressed, the profiles of inferred
294 DF curves were shifted leftward in the distance–force graph (Fig. 2C; length of cylinder
295 = 15μm, and S4-V). This shift can be reasonable, if radial distribution functions under
296 compressed conditions are considered (Fig. appx 1 and SI, Appendix section 12-1). In
297 addition, in molecular science, pressure or density of particles affects profiles of DF
298 curves [14]. However, in cell biology, we think that the above compressive conditions are
299 not physiologically relevant, because cells are essentially composed of non-compressive
300 liquid and their volumes are not changed by external pressure. These trends were similarly
301 detected under spherical spatial constraints (Fig. S4-IV). These results suggest that
302 inferred DF curves are not significantly affected by spatial constraints corresponding to
303 egg shells.

304 Next, we introduced spatial constraints corresponding to cavities. We assumed
305 that particles located on the surface of a cavity cannot penetrate into the cavity (Fig. 2D,
306 S4-VI, SI, Section 7-4-2, and Movie S8J-K). Inferred DF curves were almost consistent
307 with the DF curves from the LJ potential (Fig. 2D, S4-VI, and SI, Section 4-4). However,
308 we detected additional repulsive forces at distant regions, which we call distant energy
309 barrier (DEB). Repulsive forces around the corresponding distances were also detected
310 in DF curves inferred from simulation data where the forces between cell–cell interactions

311 were assumed to be absent but the cavities to be present (Fig. S4-VI-E, and SI, Section 4-
312 4), suggesting that DEB was derived from the cavities. Interestingly, profiles similar to
313 DEB are well-known in molecular and colloidal sciences: by considering hydration of
314 particles by solvents as an external factor, effective potentials are modified so as to
315 contain energy barriers around distant regions [1,2]. We conclude that the effects of cavities
316 can be incorporated into effective potential of cell–cell interactions. In principle, the
317 primary effect of a cavity would be to provide potential of positions for each cell but not
318 potential of cell–cell interactions. Thus, a cavity indirectly affects the effective potential
319 of cell–cell interactions. To avoid confusion in usage of the terms, we call inferred
320 potential of cell–cell interactions "effective potential for each cell modeled as cell–cell
321 interactions".
322
323 *Validation of inference method by using non-adhesive cells*
324 Before applying our inference method to three-dimensional multi-cellular
325 systems, we performed an additional negative control experiment using two-
326 dimensionally cultured cells that exhibit negligible cell–cell interactions but exert traction
327 forces between the cells and substrate, leading to random–walk-like movements. We
328 knocked out cadherin function in MDCK cells (E-cadherin and cadherin-6 in the case of

329 MDCK cells) by disrupting the gene encoding α-catenin, an essential regulator of the two
330 cadherins (Fig. S5 and SI, Section 8-3) [40]. We found that, in contrast to wild-type MDCK
331 cells which had organized DF curves (Fig. S5B), DF curves obtained from the α-catenin
332 mutant cells were disorganized (Fig. S5A), similar to those obtained from random–walk
333 simulations. This result supports the idea that our method is accurate enough to infer
334 intercellular forces in multi-cellular systems.
335
336 *Inference of effective forces in C. elegans early embryo*
337 We next investigated whether effective potential could be detected as a function
338 of cell–cell distance in three-dimensional systems. The nematode *C. elegans* has well-
339 defined embryogenesis: cell movements in early embryos are almost identical among
340 different individuals, and the time series of nuclear positions have been reported
341 previously [32]. In addition, the spatiotemporal patterns of cell differentiation are absolutely
342 the same: cell lineage and cell fate are invariant. During early *C. elegans* embryogenesis,
343 a fertilized egg (i.e., one cell) repeatedly undergoes cell division and cell differentiation,
344 ultimately forming an ovoid embryo containing ~350 cells (Fig. S6A and Movie S3A).
345 The cells become smaller through cell division [41], and the total volume of the embryo
346 remains constant because the embryo is packed into a stiff egg shell. Thus, the volume of

347 each cell is reduced by a factor of 350 relative to the original egg, meaning that cell
348 diameter is reduced by a factor of 7. Because particle diameter is approximately reflected
349 on a DF curve as the distance with force = 0 (Fig. 1B and S2D) corresponding to the
350 minimum of the potential, we expected that inferred DF curves should be gradually
351 shifted to the left side of the distance–force graph throughout embryogenesis.

352 Figure 3A is a snapshot that shows nuclear positions and inferred effective forces
353 in the embryo; the temporal change is also visualized (Fig. S6B and Movie S3B), where
354 dynamic changes in the effective forces were observed. Importantly, almost identical
355 values of the effective forces were obtained from different initial values during the
356 minimization process of Equation S6 described previously (Fig. 3B, S10A, and SI,
357 Section 4-4), suggesting that our inference problem may have a unique solution. To
358 investigate whether DF curves change during the embryogenesis, we divided the whole
359 embryogenesis into segments containing different time frames, and plotted the inferred
360 forces against the distances for each segment (Fig. 3C and S6C, time frame = 16–55, 36–
361 75, 76–115, 116–155, and 156–195). The plots were widely distributed in all the segments,
362 but the DF curves generated by averaging in each shallow bin of the distances exhibited
363 organized patterns. This was in striking contrast to the results of the random–walk
364 simulations and the α-catenin mutant cells. All of the DF curves had very similar profiles:

repulsive and attractive forces were detected around the core of the cells and longer interaction distances, respectively (Fig. 3D). The repulsive forces are likely to be derived from the volume effect of the cells, and the attractive forces might be derived from cell-cell adhesion. These patterns are typical in various non-living particle–particle interactions such as atoms and molecules, whose potentials are given by the LJ potential, etc. (Fig. S3A). We also calculated the distance–potential (DP) curves by integrating the force values; potential energy is obtained from the integral of forces along distances (Fig. 1B, S2D, and SI, Section 5). Importantly, the distances in the minimum of the effective potentials were gradually shifted toward the left side (Fig. 3D), as we had expected (Fig. 3E), indicating that the inferred effective potentials were consistent with the reduction in cell volume during embryogenesis (Fig. 3E). Taken together, the patterns of the DP curves seem to be physically reasonable. As speculated from the previous analyses using artificial simulation data (Fig. 2C), we think that the eggshell does not significantly affect the profiles of the DP curves. In addition, the data points were widely distributed from the DF curves as shown by the heat maps, which may originate in biological properties, including variety of cell sizes, the intrinsic heterogeneity of cells and/or experimental or methodological errors during detection of cell centers or the inferring process, as discussed in SI (Section 4-6).

383

384 *Effect of inferred distance–force curves on C.elegans embryonic morphologies*

385 The inferred DF curves for *C. elegans* embryogenesis seem to be reasonable.
386 However, one concern may be that the averaged DF curves are oversimplification, given
387 the broad distribution of the effective force, as discussed later. This prompted us to further
388 investigate whether the simple DF curves can explain embryonic morphologies. Because
389 the dynamics of all cells during embryogenesis are very complicated, largely due to the
390 repeated cell division and cell differentiation, we focused on a few typical features of the
391 morphologies: aggregated cells and the ovoid embryo shape. The embryonic cells can
392 keep a cell aggregate even when the eggshell is removed, and subsequent culture leads to
393 a cell aggregate with an ovoid or distorted shape, except for very early stage of
394 development (< ~20 cells) [42,43].

395 We performed simulations based on the particle-based cell model by considering
396 the DF curves, and investigated whether aggregated states with ovoid shapes were stable.
397 In multi-cellular systems, morphologies of systems are determined by both DF curves and
398 initial configurations, because energetic local minimum states (i.e. metastable state) as
399 well as global minimum states are meaningful (SI, Appendix 12-2 and Fig. appx 2). To
400 find stable states under the DF curves, we performed simulations starting from various

401 initial configurations of the particles, and the systems were relaxed. When we used the
402 DF curves obtained from the *C. elegans* embryos, we observed a tendency for the particles
403 to aggregate with an ovoid or distorted shape (Fig. 6A and S11). As a control simulation,
404 we utilized the LJ potential, and found that it did not generate an ovoid or spherical shape,
405 but rather a shape similar to its initial configuration (Fig. S11). Moreover, the FH
406 potentials generated a spherical but not ovoid shape, and the outcomes were not
407 significantly affected by the initial configurations (Fig. S11). These results suggest that
408 the inferred effective DF curves are capable of recapitulating the basic morphology of the
409 *C. elegans* embryos.
410
411 *Inference of effective force in mouse pre-implantation embryos*
412 To further investigate whether effective forces could be obtained in three-
413 dimensional systems, we focused on mouse pre-implantation embryos, including morulae
414 at the 8-cell and compaction stages, as well as blastocysts bearing cavities (Fig. 4A,
415 illustration). These embryos are surrounded by a spherical egg shell–like structure called
416 the zona pellucida, but even if that structure is removed, the embryos maintain their
417 spherical shapes and development normally [44]. In 8-cell stage embryos before compaction,
418 cell–cell adhesion is weak, and individual cells can be easily discerned (Fig. 4A, bright

field). In the compaction-stage embryos composed of ~16-32 cells, cell–cell adhesion becomes stronger due to elevated expression of cadherin proteins on cell membrane, and the cells are strongly assembled [45]. The surface of the embryo becomes smooth, and the embryonic shape becomes more spherical (Fig. 4A, bright field). In blastocyst-stage embryos composed of >64 cells, an inner cavity is formed, and the embryos expand while maintaining their spherical shape. Trophectoderm (TE) cells form a single–cell-layered structure at the outermost surface of the embryo, whereas the cells of the inner cell mass (ICM) were tightly assembled, forming a cluster (Fig. 4A, illustration). Using confocal microscopy, we performed live imaging of fluorescently labeled nuclei, obtained time series of the nuclear positions (Fig. 4A, Movie S4A-C, and SI, Section 8-1), and then applied the inference method.

Figure 4B shows the snapshots of the inferred effective forces of cell–cell interactions during the three embryonic stages that we examined (Movie S4D–G). The uniqueness of the solutions was confirmed (Fig. S10). We calculated the DF and DP curves in a manner similar to *C. elegans* study described above, and obtained curves for all three stages (Fig. 4C and D). The DF curves derived from the 8-cell and compaction stages had typical profiles, with repulsive and attractive forces detected at short and long interaction distances, respectively (Fig. 4D and S6D). On the other hand, the DF curves

437 derived from the blastocyst stage contained DEB (Fig. 4D, arrows), similar to the case of
438 artificial simulation data considering a cavity (Fig. 2D and S4-VI). Thus, we think that
439 the DEBs in the blastocysts are derived from the cavities. Such DEBs have not been
440 discovered in multi-cellular systems. Together, these results indicate that the profile of
441 DF curves changes during the development. Moreover, the profiles of the DF curves
442 suggest the consistency with previous experimental knowledge as discussed in Figure S7.
443
444 *Effect of inferred distance–force curves on mouse embryonic morphologies*
445 We next asked whether the temporally evolved DF curves derived from the
446 mouse embryos were sufficient to explain the key morphological features of the embryos.
447 Using the DF curves, we searched for stable states by an approach similar to the one we
448 used for *C. elegans* embryos. In contrast to the case of *C. elegans* embryos, in which an
449 ovoid shape was generated, the DF curve derived from the compaction stage embryo
450 yielded a spherical shape where particles were aggregated (Fig. 6B and S11). In the case
451 of the 8-cell stage embryo, simulation results were similar to those obtained for the
452 compaction stage, except that the spherical shape seemed to be slightly distorted (Fig.
453 S11). In the case of the blastocyst stage embryo, when aggregated particles were given as
454 initial configurations, the particles gradually scattered and formed a spherical structure

455 harboring a cavity at the center (Fig. 6B). We then examined whether DEB contribute to
456 the formation of a cavity. We artificially eliminated DEB from the inferred DF curves,
457 and performed a simulation. We found that no cavity was generated (Fig. 6B). These
458 results suggest that all of the DF curves from the various embryonic stages are sufficient
459 to explain their different morphologies. We also showed DF curves that were obtained
460 from interactions between adjacent cells (Fig. S8), by which we may evaluate direct cell–
461 cell interactions excluding indirect effect of cavities. Later we will discuss the differences
462 in the DF curves between the two cell populations TE and ICM (Fig. S7). We will also
463 discuss cellular polarities, such as apico-basal and planar cell polarities that were not
464 explicitly considered in this study (Fig. S9 and SI, Appendix section 12-1).
465
466 *Inference of effective distance–force curves and their effect on morphology in MDCK cyst*
467 The above results led us to hypothesize that DEB of the DF curves plays essential
468 roles in the morphogenesis of structures harboring cavities. To examine this hypothesis,
469 we focused on another system with a cavity. MDCK cells, derived from dog kidney
470 epithelium, can form cysts containing a cavity when cultured in suspension (Fig. 5A,
471 illustration) or in gels composed of extracellular matrix [46]. To exclude mechanical
472 interactions between the cysts and the external environment, we chose suspension

473 conditions in which a cyst can be assumed to be a mechanically isolated system for which
474 external forces are negligible. We obtained time series of the nuclear positions of the cysts
475 by a procedure similar to the one used for the mouse embryos (Fig. 5A, Movie S5A, and
476 SI, Section 8-2). We then inferred the effective forces and calculated the DF curves (Fig.
477 5B–D and S6E). The uniqueness of the solutions was confirmed (Fig. S10). Figure 5D
478 shows the DF and DP curves from a MDCK cyst. We found a DEB in the DF curves,
479 implying that a DEB is generally involved in morphogenesis of cavity-bearing structures.
480 Simulations based on inferred DF curves revealed that, a cavity was stably
481 maintained in MDCK cells (Fig. 6C and S11). Moreover, the DF curves from which the
482 DEB was artificially eliminated could not maintain the cavity-bearing structure (Fig. 6C).
483 Taken together, these findings indicated that the DEBs in the blastocyst and the MDCK
484 cyst play roles in the formation and maintenance of a cavity, respectively.
485
486 *Modeling of distance–force curves*
487 The analyses from the blastocysts and MDCK cysts suggest that the effect of
488 cavities can be incorporated into effective potential for each cell modeled as cell–cell
489 interactions. We hypothesized that the DF curves incorporating such external factors
490 represent a rule capable of explaining various morphogenetic events. Moreover, the

profiles of the DF curves in Figure 3-5 were quantitatively different each other (Table S2), suggesting the quantitative differences are critical for morphogenesis. To comprehensively understand the effect of the profile of the DF curves on morphogenesis, it is necessary to model the DF curves as a simple mathematical equation. We selected the following equation as described in SI (Section 6):

$$F(D) = \varepsilon(D - D_0)^{-N} \cos\left\{\frac{2\pi(D - D_0)}{\delta}\right\}, \text{ for } D > D_0 \qquad \text{(Eq. 3)}$$

Here, F is the force, D is the distance, and N is the exponent of D, affecting the decay of the DF curves along D (X-axis). D_0 and δ affect the profile of the DF curves as shown in Figure 7A. Specifically, D_0 can transform the DF curves along D, and δ affects the wavelength of the cosine function. All parameters and variables related to lengths/distances were normalized by (δ/4), leading to generation of dimensionless parameters and variables such as $D_0^* = D_0/(\delta/4)$; usage of dimensionless parameters and variables is general technique to reduce the number of parameters. This enabled us to present simulation outcomes in two-dimensional space (D_0^* and N) in a manner similar to a phase diagram (Fig. 7).

Systematic analyses of the roles of the distal energy barriers

Using the DF curves defined by Equation 3, we systematically investigated what

kind of morphologies could be generated or stably maintained, and what kind of morphological transformation could be achieved. Here, we tried to identify possible stable states, including metastable states. We set various initial configurations of particles, performed simulations under various DF curves, and then searched for local minimum states. A cavity-bearing structure was set as the initial configuration (Fig. 7B). The simulation outcomes were categorized by their morphologies and plotted on a two-dimensional space (Fig. 7B). Examples of the morphologies and DF curves are also shown. We identified cavity-bearing structures ("cavity" and "cavity with extra particles"), cups, tubes, and lattices / aggregates as possible stable states. Multiple clusters of particles were formed or disorganized morphologies were generated which include distorted rings, etc. Importantly, when the DEBs were eliminated from the DF curves, one of the cavity-bearing structures ("cavity"), cups, or tubes were not generated (Fig. 7C), indicating that the DEBs are essential for the formation or maintenance of these structures. Next, we tried other initial configurations of particles. A two-dimensional sheet was applied as the initial configuration which corresponds to a monolayered but not multi-layered cell sheet (Fig. 8). The simulation outcomes included spherically aggregated structures, cavity-bearing structures, and two-dimensional sheets (Fig. 8A). In contrast to Figure 7B, the cavity-bearing structures were newly generated even in the absence of the

527 DEBs (Fig. 8B). DF curves were found, which can maintain the two-dimensional sheet,
528 and the maintenance was largely dependent on the DEBs (Fig. 8A vs. 8B). We confirmed
529 that the generated two-dimensional sheets were not broken by slight positional
530 fluctuations (Movie S7), indicating that the structures were stable. Thus, the DEBs are
531 essential for the maintenance of two-dimensional sheet. Other analyses considering
532 different initial configurations and/or different particle numbers are shown in Figure S12;
533 tubes were maintained by DEBs, and cell sorting in systems containing multiple types of
534 cells, which is an important phenomenon in developmental biology[3], was observed.

535 *Possible transitions among various structures*

536 The results presented above demonstrate that various structures can be formed
537 or maintained by the DF curves harboring DEBs. We next investigated whether
538 modulation of the profiles of the DF curves can induce transitions among the structures.
539 We modulated the profile of the DF curves by modifying the values of the variables in
540 Equation 3. Through trial-and-error of the modulation of the profile, we found that these
541 structures transformed each other as shown in Figure 9 and Movie S6 (SI, section 7-3):
542 e.g. aggregate → cavity → cup →tube → aggregate, etc.

543

544 *Combination of inference method with traction force microscopy*

We have been showing that some external factors, such as cavities, can be incorporated into effective potentials for each cell modeled as cell–cell interactions. An alternative approach is to subtract external effects prior to inference of effective potentials, which can lead to acquisition of potentials derived from direct effects of cell–cell interactions. In other words, external effects are quantitatively measured to exclude them from inference of effective potentials. However, this kind of quantitative measurements is still challenging in biology especially in three-dimensional situations. Alternatively, we tested this approach in two-dimensional situations where traction forces are exerted between cells and substrate, because there is a well-established method to quantitatively measure traction forces, traction force microscopy (TFM) [47–50].

First, we tried this approach by using artificially generated simulation data where traction forces were provided (Fig. S13 and Movie S9). By subtract traction forces prior to inference, we obtained DF curves consistent with the given DF curve derived from the LJ potential (Fig. S13). Finally, we tried this approach in two-dimensionally cultured MDCK cells with TFM measurement (Fig. S14). Without the subtraction of traction forces, the inferred forces of cell–cell interactions were shifted toward repulsive forces. On the other hand, by subtracting traction forces, we obtained typical DF curves with repulsive forces at shorter distance and attractive forces at middle distances (Fig. S13 and

563 S14). These results suggest that, by combination with TFM and possibly other techniques,
564 our inference method can yield potentials derived from direct effects of cell–cell
565 interactions.
566
567 *Extraction of information of cell polarity*
568 We have been inferring effective potentials for each cell modeled as cell–cell
569 interactions without explicitly considering cell polarities such as apico-basal polarities
570 and polarities on cell sheet including planar cell polarity (PCP). We tried to extract these
571 polarities from the inferred effective potentials by considering directions of cell–cell
572 interactions.
573 First, we analyzed the inference results derived from artificially generated
574 simulation data with unidirectional traction forces under two-dimensional situations as
575 previously shown (Fig. S13G and S13H). In this simulation, the leading cells exerted the
576 largest traction forces among all cells, and the traction force values were gradually
577 decreased from the leading cells to the followers. This situation resembles wound healing.
578 Thus, the cells have polarities on the cell sheet: the direction of collective migration vs.
579 its vertical direction. We divided the directions of cell–cell interactions into three
580 categories according to their angles, and tested whether DF curves obtained from these

581 categories became different each other. Note that we did not subtract traction forces in
582 this analysis. As shown in Figure S15, the DF curve along the vertical direction of
583 collective migration was equivalent to the DF curve derived from the LJ potential,
584 whereas the DF curve along the direction of collective migration was significantly
585 changed, resulting in a repulsive force-dominant profile. This is intuitively reasonable,
586 because cell–cell distances along the direction of collective migration are increased
587 during wound healing, which corresponds to existence of apparent repulsive forces. These
588 results suggest that cell polarity can be extracted after inferring effective potentials. Note
589 that the inferred effective potentials contain parts of the effects of external forces but not
590 all: external forces such as traction forces can move the centroid of cell populations but
591 internal forces such as the effective potentials modeled as cell–cell interactions cannot
592 due to the law of conservation of momentum.

593 We also tried to extract cell polarity in mouse embryos. During the compaction
594 stage, the cells, which are located on the outer surface of the embryos, gradually form cell
595 polarity [51], leading to the differences in protein localization between the junctions of
596 outer–outer cells and of outer–inner cells. We found that the DF curves of these two
597 interactions were different each other (Fig. S7A). Finally, we analyzed apico-basal
598 polarity in TE cells of mouse blastocyst. We tried to extract DF curves in the cell sheet of

599 TE and along the direction vertical to the cell sheet corresponding to the apico-basal
600 direction. However, there were essentially no cell–cell interactions detected along the
601 apico-basal direction, as shown by the probability of cell distribution against the
602 directions (Fig. S9A-C). Thus, we cannot infer DF curve along the apico-basal direction.
603 In general, probability of states is linked to potential energy (SI, Appendix section 12-1).
604 Thus, we calculated potential energies against the angular direction, and found that the
605 potential energy along the apico-basal was expected to be extremely large compared with
606 the direction on the cell sheet (Fig. S9D and S15D).
607
608 *Influence of experimental noise on inference result*
609 In general, accuracy of inference methods can be affected by observation noises.
610 In our method, noises of nuclear positions during image recognition may affect the
611 accuracy. We theoretically assessed the influence of the noises of nuclear positions (SI,
612 Section 4-5). Using artificially generated simulation data, we added noises of nuclear
613 positions as Gaussian noises, and inferred effective potentials for each cell modeled as
614 cell–cell interactions. The averaged distances between nuclear positions before and after
615 adding Gaussian noises was set variously from 0.16 to 1.0μm (Table S1-i-iv). We found
616 that the increase in the Gaussian noises caused modulation of inferred DF curves (Table

617 S1-i-iv and Movie S10). There were two major modulations: an emergence of
618 disorganized patterns similar to that from random walk and an increase in maximum
619 absolute values of attractive forces (Table S1-i-iv and SI, Section 4-5). In spite of the
620 latter modulation, the peaks of attractive forces were not significantly changed along the
621 distances, suggesting that overall patterns were almost conserved except for the absolute
622 values of attractive forces. It is difficult to correctly estimate actual experimental noises,
623 but residuals from smoothing spline interpolation along time for positions of each nucleus
624 might roughly correspond to experimental noises (Fig. appx 4 and SI, Appendix section
625 12-4). We found that the values of the residuals ranged from 0.2 to 0.4μm in the *C. elegans*
626 embryo, the mouse embryos, and the MDCK cysts (SI, Section 4-5-2). As shown in Table
627 S1-i-iv, these *in vivo* situations fell within acceptable conditions expected from the
628 artificial data: the patterns of DF curves would not be disorganized/randomized and the
629 orders of the absolute values of attractive forces are expected to be sustained.
630
631
632 Discussion
633 In this study, we developed a method for statistically inferring effective forces
634 of cell–cell interactions using nuclear tracking data obtained from microscopic images.

We then demonstrated that effective potentials for each cell modeled as cell–cell interactions can be extracted from the inferred forces in various living systems. Our findings provide for the first time the experimental quantification of effective potentials, which have been recognized conceptually [11,17]. We also showed that, in the coarse-grained cellular model, the effective potentials can partially contain information of cell polarities and of external factors such as cavities, which can be decoded after inference, suggesting that the effective potential is an integrative parameter. By considering the effective potentials, we successfully reproduced various three-dimensional structures, including cell aggregates, cavity-bearing structures, cups, tubes, two-dimensional sheets, and sorted cells. These structures are often observed during embryogenesis, morphogenesis, and organoids prior to the formation of complex tissue structures. For instance, cell aggregates are observed in early embryos in various species and spheroids [20,32,52–57]; cavity-bearing structures in early embryos of various species, organoids, and cystic diseases [46,52,58–61]; cell sheets in epithelia and germ layers [20,56,62–65]; tubes in tubular organs [66–68]; and cups in retina (i.e. optic cup) and murine epiblast [53,69]. Thus, we consider these structure as basic structural units for morphogenesis. These results suggest that the effective potentials alone are powerful to explain diverse three-dimensional morphologies. Although cell–cell interactions are affected by many parameters including proteins such as cadherins

653 and cellular structures such as actomyosin cytoskeletons (Fig. S1 and S5), we suppose
654 that the effective potentials in the coarse-grained model can be an integrative and unifying
655 mesoscopic parameter to explain morphogenetic events. Our goal is to develop a
656 framework for explaining diverse morphogenesis in a minimal model. The model based
657 on effective potential represents such a framework with few degrees of freedom (Fig.
658 S1A), and this provides a novel paradigm for understanding the morphogenesis of multi-
659 cellular systems and their morphological evolution. We believe that effective potentials
660 and the inference method constitute a powerful approach for exploring principles for
661 diverse morphogenesis.
662
663 *Profile of effective potentials of cell–cell interaction*
664 We discovered distant energy barriers (DEBs) in the effective potentials obtained
665 from blastocysts and MDCK cysts, which would be derived from indirect effect of
666 cavities. These energy barriers contributed significantly to the generation and
667 maintenance of cavity-bearing structures, tubes, and sheets. Such energy barriers are well-
668 known in molecular and colloidal sciences, as mentioned in SI (Section 5-4-1). We
669 speculate the physical interpretation of these energy barriers in cells below. In the case of
670 the blastocysts, the trophectoderm cells form tight junction to seal gaps between the cells

671 and transport liquid from the outside of the embryos to the cavities, resulting in increased
672 hydrostatic pressure, fracturing of the cell–cell contacts of the inner cells, and subsequent
673 expansion of the cavities [70–72]. Therefore, the TE cells push each other through the liquid
674 in the cavities. This indirect mechanical repulsion might be reflected in the DEBs (Fig.
675 S16A). In the case of the MDCK cysts, tubes, and sheets, the DEBs may reflect properties
676 of cell sheets as discussed in Figure S16B.
677
678 Potentials of cell–cell interactions have been widely considered in various
679 materials such as active matter including self-migratory cells. In these studies, however,
680 the profiles of the distance–potential curves are assumed without experimental bases. For
681 instance, hard- or soft-core, square-well, JKR, and other potentials have been considered
682 (Fig. appx 5 and SI, Appendix section 12-5) [19,20,25,73,74]. Animal and human behaviors can
683 also be modeled as active matter governed by attractive and repulsive interactions [75–78].
684 Our inference method can be used to obtain the profiles of the potentials in these materials,
685 possibly leading to new finding of the dynamics of these materials. Moreover, the material
686 properties of particulate soft matter can be estimated using inferred effective potentials as
687 demonstrated in SI (Fig. S17, Table S2, and SI, Section 4-6-2 and 5-4-2).
688

Usefulness, application, and limitation of inference method

Our *in situ* inferences provide information about mechanical states, or maps, of living systems. Various methods have been developed for measuring or inferring mechanical maps in living systems such as TFM (Fig. S14) [17,37,79–82]. Our method is advantageous for obtaining mechanical states in three-dimensional situations with temporal evolution. To understand mechanical states, it is necessary to complementary utilize these methods with various temporal and spatial resolutions, as demonstrated by combining our method with TFM (Fig. S14).

To understand morphogenetic events, mechanical states and simulations based on those states are essential. Models such as vertex and Cellular Potts models are often utilized, especially for epithelial cells, where the cells are modeled as polygonal or polyhedral shapes with adhesion energy and surface tension [5,52,58]. These models successfully recapitulated various morphogenetic events, including the formation of the mouse blastocyst [52], very early embryogenesis in *C.elegans* [83], and the formation of cystic structures in kidney [58]. These models often contain non-cellular components such as liquid in cavities and egg shells. However, it is still challenging to measure cellular and non-cellular parameters in three-dimensional systems with high spatiotemporal resolution (e.g. spatiotemporal information of pressure of cavities, and traction forces in three-

707 dimensional situations), although high-resolution inference has been performed in two-
708 dimensional situations [37,82]. This means that there is no clear way to connect the model
709 parameters to *in vivo* ones in three-dimensional systems. On the other hand, particle-based
710 cellular models can also assume parameters other than the potential of cell–cell
711 interactions, leading to recapitulation of complex three-dimensional structures such as the
712 blastocyst [84–86]. In particular, a recent study reported a model that considered cell
713 polarities, in which transformation from cell aggregates to cell sheets and bending of cell
714 sheets were simulated [86]. Particle-based models have also been expanded by considering
715 cell shapes, where a cell is composed of two particles or a Voronoi tessellation is
716 combined to implement multibody effect [22,28,31,57,63,87,88], and mechanical properties and
717 dynamics of self-propelled cells or cell aggregates were investigated. These observations
718 suggest that particle-based models are potentially applicable to very complex structures,
719 although it has not been established whether highly deformed cells and non-cellular
720 structures such as extracellular matrix can be implemented simply in particle-based
721 models. In our strategy, model parameters inferred from *in vivo* systems can be used for
722 simulations. Our method provides a framework for quantitatively connecting model
723 parameters to *in vivo* parameters under three-dimensional situations, and will thus be
724 complementary to other models.

725 Investigations of the origins of the effective potentials are important for a
726 complete understanding of morphogenesis. Various proteins including cadherins and
727 actomyosins should be involved in the potentials. In fact, disruption of the gene encoding
728 α-catenin, which is essential for the function of cadherin proteins, leads to the changes in
729 the profile of effective potentials (Fig. S5). Our framework enables us to relate proteins
730 to the profile of potentials by evaluating the effect of gene disruption or inhibition on the
731 profile. Comprehensive evaluation of the effect of various proteins will be valuable, and
732 will provide a bridge between the physics of morphogenesis and molecular biology.
733
734 *Toward understanding of a later stage of embryogenesis and organogenesis*
735 In this study, we used relatively small embryos: mouse pre-implantation embryos
736 (several tens of cells) and the *C. elegans* embryo (< 350 cells). To apply our inference
737 method and simulation model to later embryonic stages, new components should be
738 considered, such as the increase in the number of cell types, cell polarities, and
739 chemotaxis. The number of cell types increases through cell differentiation, in which
740 mesenchymal cells as well as blastomere cells and epithelial cells are included. The
741 blastocyst contains at least two cell types (ICM and TE), and we successfully detected the
742 differences in the DF curves between these two cell types (Fig. S7). In later stages of

743 embryogenesis, such as gastrulation, the embryos are usually composed of mixtures of
744 mesenchymal and epithelial cells, in which the epithelial-to-mesenchymal transition
745 occurs. In contrast to the vertex model, where mesenchymal cells cannot be considered,
746 particle-based models may simulate the mesenchymal cells and mixtures of mesenchymal
747 and epithelial cells [24,25]. Mesenchymal and epithelial cells are separated each other (i.e.
748 cell sorting), which has been explained by differential cell–cell adhesiveness [3]. Other
749 group and we demonstrated that particle-based models can reproduce cell sorting by
750 considering cell–cell adhesiveness as potentials (Fig. S12-III-B) [89]. Apico-basal and
751 planar cell polarities are critical parameters for morphogenesis [86]. We speculate that these
752 polarities can be implemented in the particle model by implementing two particles for a
753 cell where cell shapes become anisotropic [28,31], or by considering directional differences
754 in the profiles of effective potentials, as recently proven by other group [86] and shown in
755 Figure S7A and S15D. Cell–cell interactions are regulated not only by mechanical forces
756 but also by chemical signaling such as chemotaxis and ephrin proteins (Fig. S1B). By
757 expanding the concept of effective potentials, we think that attractive and repulsive effects
758 of chemical signaling can be implemented as the profile of the effective potentials,
759 possibly with non-reciprocal interactions [90–94]. It is possible that by analyzing inferred
760 cell–cell interaction forces, we could extract differences in cell types, directional

differences in the profile of the effective potentials, and the effects of chemotaxis.

At this moment, we do not know whether the particle-based model is useful for later stages of embryogenesis or larger tissues to which continuum models are usually applied [95]. Multi-scale frameworks may be required to connect particle-based models with continuum models based on macroscopic parameters. In any case, our inference method may be useful for evaluating material properties of larger tissues, which are essential for developing continuum models.

Conclusion

Our framework, composed of the inference method and the particle-based model, has various potential uses for investigating the properties of cell–cell interaction, single-cell analysis of mechanics, material properties, mechanical maps, three-dimensional morphogenesis, relationships between mechanical parameters and gene products, and comparisons of mechanical parameters and behaviors among different living species and non-living systems. Although some of these issues will be examined in the future, we propose that our framework provides a novel physical scenario for understanding the biophysics and physical biology of diverse morphogenetic events.

Experimental materials and methods

Mouse embryos were obtained by mating Rosa26-H2B-EGFP knock-in male mice [36] with ICR female mice. Animal care and experiments were conducted in accordance with the Guidelines of Animal Experiment of the National Institutes of Natural Sciences. Experiments were approved by the Institutional Animal Care and Use Committee of the National Institutes of Natural Sciences. MDCK transgenic cells bearing H2B-EGFP were generated using a piggy-bac plasmid [96,97]. α-catenin mutant cells were constructed previously [98]. The detailed procedures for cell and embryo cultures, microscopic imaging, nuclear tracking, force inference, simulations, and data analyses are described in SI. The nuclear tracking data, inferred forces, and profiles of distance–force curves are provided in SI. TFM was performed as described previously [48,49].

Acknowledgement

We thank Drs. Hitoshi Niwa and Yayoi Toyooka for providing the piggy-bac plasmids and technical suggestions. We thank Drs. Jean-François Joanny, Hiroaki Takagi and Yasuhiro Inoue for critical reading of the manuscript. We thank Drs. Kazuhiro Aoki and

Yohei Kondo for kindly providing images for TFM and critical suggestions about TFM. We thank Dr. Yoshitaka Kimori for helpful discussions. We thank Ms. Azusa Kato for supporting nuclear tracking. This work was supported by following grants: Japan Ministry of Education, Culture, Sports, Science and Technology Grant-in-Aid for Scientific Research on Innovative Areas "Cross-talk between moving cells and microenvironment as a basis of emerging order" for H.K., the National Institutes of Natural Sciences (NINS) program for cross-disciplinary science study for H.K., a Japan Society for the Promotion of Science (JSPS) Grant-in-Aid for Young Scientists (B) for H.K. (17K15131), for Scientific Research (C) for T.O. (18K06234), and for Young Scientists (B) for T.O. (16K18544), a MEXT/JSPS Grant-in-Aid for Scientific Research on Innovative Areas for T.O. (17H05627), the Inamori Foundation for T.O., and the Takeda Science Foundation for T.O.

Conflicts of interest

The authors declare no competing financial interests.

Author contribution

H.K. designed the work, H.K., A.M.I., and H.O. contributed to the conception. H.K. and

T.F. designed experiments, T.O. provided experimental materials, and H.K. performed experiments and image processing. H.K. and H.O. designed models, H.K. developed computational algorithms, and H.K. and K.N. statistically analyzed the data. H.K., T.O., H.O., A.M.I., K.N., K.K., and T.F. wrote the manuscript, and all authors contributed to the interpretation of the results.

References

1. Pettitt, B. M. & Rossky, P. J. Alkali halides in water: Ion–solvent correlations and ion–ion potentials of mean force at infinite dilution. *J. Chem. Phys.* **84**, 5836–5844 (1986).
2. Israelachvili, J. N. *Intermolecular and Surface Forces*. (Elsevier Inc., 2011).
3. Steinberg, M. S. Differential adhesion in morphogenesis : a modern view. *Curr. Opin. Genet. Dev.* **17**, 1281–286 (2007).
4. Guillot, C. & Lecuit, T. Mechanics of epithelial tissue homeostasis and morphogenesis. *Science (80-.).* **340**, 1185–9 (2013).
5. Fletcher, A. G., Osterfield, M., Baker, R. E. & Shvartsman, S. Y. Vertex models of epithelial morphogenesis. *Biophys. J.* **106**, 2291–2304 (2014).
6. Maître, J.-L. *et al.* Adhesion Functions in Cell Sorting by Mechanically Coupling

the Cortices of Adhering Cells. *Science (80-.).* **338**, 253–256 (2012).

7. Bazellières, E. *et al.* Control of cell–cell forces and collective cell dynamics by the intercellular adhesome. *Nat. Cell Biol.* **17**, 409–420 (2015).

8. Yong, J. *et al.* Spatial distribution of cell–cell and cell–ECM adhesions regulates force balance while maintaining E-cadherin molecular tension in cell pairs. *Mol. Biol. Cell* **26**, 2456–2465 (2015).

9. Manning, M. L., Foty, R. A., Steinberg, M. S. & Schoetz, E.-M. Coaction of intercellular adhesion and cortical tension specifies tissue surface tension. *Proc. Natl. Acad. Sci.* **107**, 12517–12522 (2010).

10. David, R. *et al.* Tissue cohesion and the mechanics of cell rearrangement. *Development* **141**, 3672–3682 (2014).

11. Forgacs, G. & Newman, S. A. *Biological Physics of the Developing Embryo*. (Cambridge University Press, 2005).

12. Ma, X. *et al.* Fibers in the extracellular matrix enable long-range stress transmission between cells. *Biophys. J.* **104**, 1410–1418 (2013).

13. Li, X. *et al.* On the mechanism of long-range orientational order of fibroblasts. *Proc. Natl. Acad. Sci.* **114**, 8974–8979 (2017).

14. Atkins, P., Paula, J. De & Keeler, J. *Atkins' Physical Chemistry*. (Oxford

University Press, 2018).

15. Ito, A. M., Takayama, A., Saito, S. & Nakamura, H. Formation and Classification of Amorphous Carbon by Molecular Dynamics Simulation. *Jpn. J. Appl. Phys.* **52**, 01AL04 (2013).

16. Frenkel, D. & Smit, B. *Understanding Molecular Simulation*. (Academic Press, 2002).

17. Merkel, M. & Manning, M. L. Using cell deformation and motion to predict forces and collective behavior in morphogenesis. *Semin. Cell Dev. Biol.* **67**, 161–169 (2017).

18. Weikl, T. R., Asfaw, M., Krobath, H., Bartosz, R. & Lipowsky, R. Adhesion of membranes via receptor–ligand complexes: Domain formation, binding cooperativity, and active processes. *Soft Matter* **5**, 3213–3224 (2009).

19. Drasdo, D., Kree, R. & McCaskill, J. S. Monte Carlo approach to tissue-cell populations. *Phys. Rev. E* **52**, 6635–6657 (1995).

20. Drasdo, D. & Höhme, S. A single-cell-based model of tumor growth in vitro: monolayers and spheroids. *Phys. Biol.* **2**, 133–147 (2005).

21. Yamao, M., Naoki, H. & Ishii, S. Multi-cellular logistics of collective cell migration. *PLoS One* **6**, (2011).

22. Ranft, J. *et al.* Fluidization of tissues by cell division and apoptosis. *Proc. Natl. Acad. Sci. U. S. A.* **107**, 20863–20868 (2010).

23. Sepúlveda, N. *et al.* Collective Cell Motion in an Epithelial Sheet Can Be Quantitatively Described by a Stochastic Interacting Particle Model. *PLoS Comput. Biol.* **9**, e1002944 (2013).

24. Arboleda-Estudillo, Y. *et al.* Movement Directionality in Collective Migration of Germ Layer Progenitors. *Curr. Biol.* **20**, 161–169 (2010).

25. Szabó, B. *et al.* Phase transition in the collective migration of tissue cells: Experiment and model. *Phys. Rev. E* **74**, 061908 (2006).

26. Kashef, J. & Franz, C. M. Quantitative methods for analyzing cell–cell adhesion in development. *Dev. Biol.* **401**, 165–174 (2015).

27. Garcia, S. *et al.* Physics of active jamming during collective cellular motion in a monolayer. *Proc. Natl. Acad. Sci. U. S. A.* **112**, 15314–15319 (2015).

28. Basan, M., Elgeti, J., Hannezo, E., Rappel, W.-J. & Levine, H. Alignment of cellular motility forces with tissue flow as a mechanism for efficient wound healing. *Proc. Natl. Acad. Sci.* **110**, 2452–2459 (2013).

29. Schötz, E. *et al.* Quantitative differences in tissue surface tension influence zebrafish germ layer positioning. *HFSP J.* **2**, 42–56 (2008).

30. He, B., Doubrovinski, K., Polyakov, O. & Wieschaus, E. Apical constriction drives tissue-scale hydrodynamic flow to mediate cell elongation. *Nature* **508**, 392–396 (2014).

31. Basan, M., Prost, J., Joanny, J.-F. & Elgeti, J. Dissipative particle dynamics simulations for biological tissues: rheology and competition. *Phys. Biol.* **8**, 026014 (2011).

32. Bao, Z. *et al.* Automated cell lineage tracing in Caenorhabditis elegans. *Proc. Natl. Acad. Sci. U. S. A.* **103**, 2707–2712 (2006).

33. McDole, K. *et al.* In Toto Imaging and Reconstruction of Post-Implantation Mouse Development at the Single-Cell Level. *Cell* **175**, 859-876.e33 (2018).

34. Amat, F. & Keller, P. J. Towards comprehensive cell lineage reconstructions in complex organisms using light-sheet microscopy. *Dev. Growth Differ.* **55**, 563–578 (2013).

35. Kyoda, K. *et al.* WDDD: Worm developmental dynamics database. *Nucleic Acids Res.* **41**, D732-7 (2013).

36. Kurotaki, Y., Hatta, K., Nakao, K., Nabeshima, Y.-I. & Fujimori, T. Blastocyst axis is specified independently of early cell lineage but aligns with the ZP shape. *Science* **316**, 719–23 (2007).

37. Ishihara, S. & Sugimura, K. Bayesian inference of force dynamics during morphogenesis. *J. Theor. Biol.* **313**, 201–211 (2012).

38. Fletcher, S. J. *Data Assimilation for the Geosciences: From Theory to Application*. (Elsevier, 2017).

39. Hirashima, T. Pattern Formation of an Epithelial Tubule by Mechanical Instability during Epididymal Development. *Cell Rep.* **9**, 866–873 (2014).

40. Hirano, S., Kimoto, N., Shimoyama, Y., Hirohashi, S. & Takeichi, M. Identification of a Neural a-Catenin as a Key Regulator of Cadherin Function and Multicellular Organization. *Cell* **70**, 293–301 (1992).

41. Arata, Y., Takagi, H., Sako, Y. & Sawa, H. Power law relationship between cell cycle duration and cell volume in the early embryonic development of Caenorhabditis elegans. *Front. Physiol.* **5**, 529 (2015).

42. Edgar, L. G. Blastomere Culture and Analysis. *Methods Cell Biol.* **48**, 303–321 (1995).

43. Schierenberg, E. & Junkersdorf, B. The role of eggshell and underlying vitelline membrane for normal pattern formation in the early C. elegans embryo. *Roux's Arch. Dev. Biol.* **202**, 10–16 (1992).

44. Motosugi, N., Bauer, T., Polanski, Z., Solter, D. & Hiiragi, T. Polarity of the

mouse embryo is established at blastocyst and is not prepatterned. *Genes Dev.* **19**, 1081–1092 (2005).

45. Fierro-González, J. C., White, M. D., Silva, J. C. & Plachta, N. Cadherin-dependent filopodia control preimplantation embryo compaction. *Nat. Cell Biol.* **15**, 1424–33 (2013).

46. Wang, A. Z., Ojakian, G. K. & Nelson, W. J. Steps in the morphogenesis of a polarized epithelium. *J. Cell Sci.* **95**, 137–152 (1990).

47. Style, R. W. *et al.* Traction force microscopy in physics and biology. *Soft Matter* **10**, 4047–4055 (2014).

48. Aoki, K. *et al.* Propagating Wave of ERK Activation Orients Collective Cell Migration. *Dev. Cell* **43**, 305–317 (2017).

49. Tseng, Q. Z. *et al.* Spatial organization of the extracellular matrix regulates cell-cell junction positioning. *Proc. Natl. Acad. Sci. U. S. A.* **109**, 1506–1511 (2012).

50. Nier, V. *et al.* Kalman Inversion Stress Microscopy. *Biophys. J.* **115**, 1808–1816 (2018).

51. Hirate, Y. & Sasaki, H. The role of angiomotin phosphorylation in the Hippo pathway during preimplantation mouse development. *Tissue barriers* **2**, e28127 (2014).

52. Honda, H., Motosugi, N., Nagai, T., Tanemura, M. & Hiiragi, T. Computer simulation of emerging asymmetry in the mouse blastocyst. *Development* **135**, 1407–1414 (2008).

53. Eiraku, M. *et al.* Self-organizing optic-cup morphogenesis in three-dimensional culture. *Nature* **472**, 51–6 (2011).

54. Marmottant, P. *et al.* The role of fluctuations and stress on the effective viscosity of cell aggregates. *Proc Natl Acad Sci U S A* **106**, 17271–17272 (2009).

55. Campàs, O. *et al.* Quantifying cell-generated mechanical forces within living embryonic tissues. *Nat. Methods* **11**, 183–9 (2014).

56. Pérez-González, C. *et al.* Active wetting of epithelial tissues. *Nat. Phys.* **15**, 79–88 (2019).

57. Montel, F. *et al.* Stress Clamp Experiments on Multicellular Tumor Spheroids. *Phys. Rev. Lett.* **107**, 188102 (2011).

58. Belmonte, J. M. *et al.* Virtual-tissue computer simulations define the roles of cell adhesion and proliferation in the onset of kidney cystic disease. *Mol. Biol. Cell* **27**, 3673–3685 (2016).

59. Kessler, M. *et al.* The Notch and Wnt pathways regulate stemness and differentiation in human fallopian tube organoids. *Nat. Commun.* **6**, 8989 (2015).

60. Rivron, N. C. *et al.* Blastocyst-like structures generated solely from stem cells. *Nature* **557**, 106–111 (2018).

61. Serra, D. *et al.* Self-organization and symmetry breaking in intestinal organoid development. *Nature* **569**, 66–72 (2019).

62. Aigouy, B. *et al.* Cell Flow Reorients the Axis of Planar Polarity in the Wing Epithelium of Drosophila. *Cell* **142**, 773–786 (2010).

63. Vitorino, P., Hammer, M., Kim, J. & Meyer, T. A Steering Model of Endothelial Sheet Migration Recapitulates Monolayer Integrity and Directed Collective Migration. *Mol. Cell. Biol.* **31**, 342–350 (2011).

64. Drasdo, D. & Forgacs, G. Modeling the interplay of generic and genetic mechanisms in cleavage, blastulation, and gastrulation. *Dev. Dyn.* **219**, 182–191 (2000).

65. Smutny, M. *et al.* Friction forces position the neural anlage. *Nat. Cell Biol.* **19**, 306–317 (2017).

66. Montesano, R., Schaller, G. & Orci, L. Induction of epithelial tubular morphogenesis in vitro by fibroblast-derived soluble factors. *Cell* **66**, 697–711 (1991).

67. Atsuta, Y. & Takahashi, Y. FGF8 coordinates tissue elongation and cell

epithelialization during early kidney tubulogenesis. *Development* **142**, 2329–2337 (2015).

68. Koyama, H. *et al.* Mechanical Regulation of Three-Dimensional Epithelial Fold Pattern Formation in the Mouse Oviduct. *Biophys. J.* **111**, 650–665 (2016).

69. Solnica-krezel, L. & Sepich, D. S. Gastrulation: Making and Shaping Germ Layers. *Annu. Rev. Cell Dev. Biol.* **28**, 687–717 (2012).

70. Moriwaki, K., Tsukita, S. & Furuse, M. Tight junctions containing claudin 4 and 6 are essential for blastocyst formation in preimplantation mouse embryos. *Dev Biol* **312**, 509–22 (2007).

71. Wang, X. *et al.* Characterizing Inner Pressure and Stiffness of Trophoblast and Inner Cell Mass of Blastocysts. *Biophys. J.* **115**, 2443–2450 (2018).

72. Dumortier, J. G. *et al.* Hydraulic fracturing and active coarsening position the lumen of the mouse blastocyst. *Science (80-.).* **365**, 465–468 (2019).

73. D'Orsogna, M. R., Chuang, Y. L., Bertozzi, A. L. & Chayes, L. S. Self-Propelled Particles with Soft-Core Interactions : Patterns , Stability , and Collapse. *Phys. Rev. Lett.* **96**, 104302 (2006).

74. Delile, J., Herrmann, M., Peyriéras, N. & Doursat, R. A cell-based computational model of early embryogenesis coupling mechanical behaviour and gene

regulation. *Nat. Commun.* **8**, 13929 (2017).

75. Shimoyama, N., Sugawara, K., Mizuguchi, T., Hayakawa, Y. & Sano, M. Collective Motion in a System of Motile Elements. *Phys. Rev. Lett.* **76**, 3870–3873 (1996).

76. Helbing, D. & Molnár, P. Social force model for pedestrian dynamics. *Phys. Rev. E* **51**, 4282–4286 (1995).

77. Couzin, I. D. & Krause, J. Self-Organization and Collective Behavior in Vertebrates. *Adv. study Behav.* **32**, 1–75 (2003).

78. Sugi, T., Ito, H., Nishimura, M. & Nagai, K. H. C. elegans collectively forms dynamical networks. *Nat. Commun.* **10**, 683 (2019).

79. Campàs, O. A toolbox to explore the mechanics of living embryonic tissues. *Semin. Cell Dev. Biol.* **55**, 119–130 (2016).

80. Serwane, F. *et al.* In vivo quantification of spatially varying mechanical properties in developing tissues. *Nat. Methods* **14**, 181–186 (2017).

81. Scarcelli, G. *et al.* Noncontact three-dimensional mapping of intracellular hydromechanical properties by Brillouin microscopy. *Nat. Methods* **12**, 1132–1134 (2015).

82. Tambe, D. T. *et al.* Collective cell guidance by cooperative intercellular forces.

Nat. Mater. **10**, 469–75 (2011).

83. Kajita, A., Yamamura, M. & Kohara, Y. Computer simulation of the cellular arrangement using physical model in early cleavage of the nematode Caenorhabditis elegans. *Bioinformatics* **19**, 704–716 (2003).

84. Krupinski, P., Chickarmane, V. & Peterson, C. Simulating the Mammalian Blastocyst - Molecular and Mechanical Interactions Pattern the Embryo. *PLoS Comput. Biol.* **7**, e1001128 (2011).

85. Nissen, S. B. *et al.* Four simple rules that are sufficient to generate the mammalian blastocyst. *PLoS Biol.* **15**, e2000737 (2017).

86. Nissen, S. B., Rønhild, S., Trusina, A. & Sneppen, K. Theoretical tool bridging cell polarities with development of robust morphologies. *Elife* **7**, e38407 (2018).

87. Bi, D., Yang, X., Marchetti, M. C. & Manning, M. L. Motility-driven glass and jamming transitions in biological tissues. *Phys. Rev. X* **6**, 021011 (2016).

88. Honda, H. Description of cellular patterns by Dirichlet domains: The two-dimensional case. *J. Theor. Biol.* **72**, 523–530 (1978).

89. Belmonte, J. M., Thomas, G. L., Brunnet, L. G., de Almeida, R. M. C. & Chate, H. Self-Propelled Particle Model for Cell-Sorting Phenomena. *Phys. Rev. Lett.* **100**, 248702 (2008).

90. Mammoto, T. *et al.* Mechanochemical Control of Mesenchymal Condensation and Embryonic Tooth Organ Formation. *Dev. Cell* **21**, 758–769 (2011).

91. Yamanaka, H. & Kondo, S. In vitro analysis suggests that difference in cell movement during direct interaction can generate various pigment patterns in vivo. *Proc. Natl. Acad. Sci.* **111**, 1867–1872 (2014).

92. Kano, T., Osuka, K., Kawakatsu, T. & Ishiguro, A. Mathematical Analysis for Non-reciprocal-interaction-based Model of Collective Behavior. *J. Phys. Soc. Japan* **86**, 124004 (2017).

93. Rodriguez-Franco, P. *et al.* Long-lived force patterns and deformation waves at repulsive epithelial boundaries. *Nat. Mater.* **16**, 1029–1036 (2017).

94. Cohen, M., Georgiou, M., Stevenson, N. L., Miodownik, M. & Baum, B. Dynamic Filopodia Transmit Intermittent Delta-Notch Signaling to Drive Pattern Refinement during Lateral Inhibition. *Dev. Cell* **19**, 78–89 (2010).

95. Shyer, A. E. *et al.* Villification: how the gut gets its villi. *Science* **342**, 212–8 (2013).

96. Nakatake, Y. *et al.* Kinetics of drug selection systems in mouse embryonic stem cells. *BMC Biotechnol.* **13**, (2013).

97. Guo, G. *et al.* Klf4 reverts developmentally programmed restriction of ground

state pluripotency. *Development* **136**, 1063–1069 (2009).

98. Otani, T. *et al.* Claudins and JAM-A coordinately regulate tight junction formation and epithelial polarity. *J. Cell Biol.* (2019) doi:10.1083/jcb.201812157.

Figures

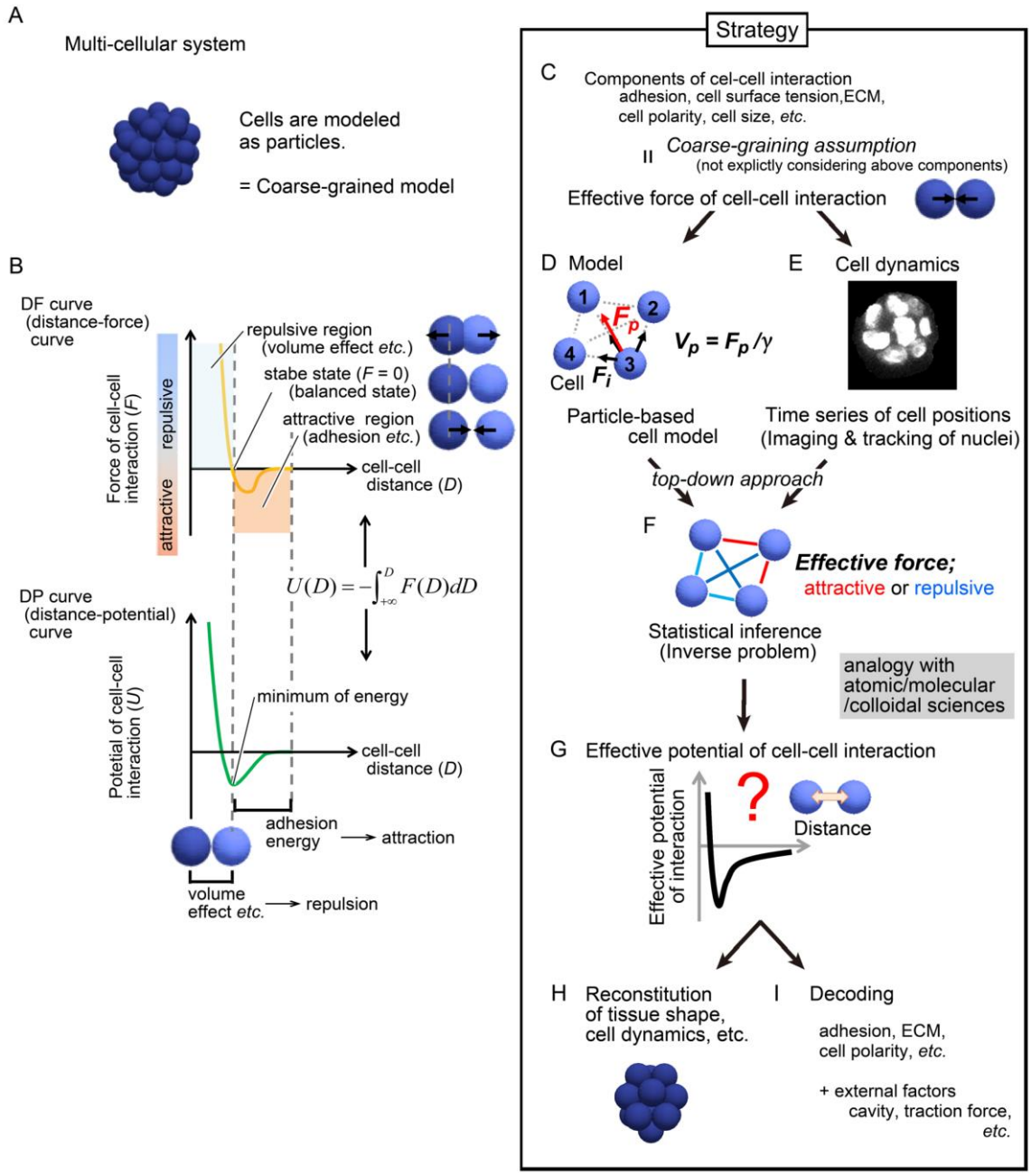

Figure 1: Overview of strategy for inferring the effective potential of cell–cell interactions A. Cells were modeled as particles. A blue sphere corresponds to a cell. B. In the particle-based model, distance–force (DF) and distance–potential (DP) curves are considered. Typical profiles of the curves, their physical meaning, and their origins are shown. DF

1065 and DP curves are mathematically transformed each other. The distance with force = 0
1066 corresponds to the distance with energetic minimum. C-I. Strategy for inferring effective
1067 forces of cell–cell interactions is described. C. Mechanics of cell–cell interactions is
1068 coarse-grained, leading to effective forces of cell–cell interactions as shown in D. There
1069 are many components related to cell–cell interactions, which are not explicitly considered
1070 in this coarse-grained model. D. In the coarse-grained model, attractive or repulsive force
1071 between the particles (blue spheres #1–4), was considered; force vectors (F_i) are
1072 illustrated by black arrows in the case of particle #3. The net force (F_p) is shown by a red
1073 vector, and the relationship between F_p and velocity (V_p) is described. E. From a time
1074 series of microscopic images of nuclei, nuclear tracking data were obtained. An image
1075 derived from a cyst formed by MDCK cells expressing H2B-EGFP is shown as an
1076 example. F. Effective forces of cell–cell interactions were inferred by solving an inverse
1077 problem: we statistically searched for force values in the model (D) that could reproduce
1078 the nuclear tracking data (E). G. The inferred force values (F) were plotted against the
1079 distance between cell–cell interactions, and whether DF or DP curves are emerged from
1080 the plots were examined. H. Whether the DF or DP curves can reconstitute tissue shape
1081 or cell dynamics was examined. I. Whether components related to cell–cell interactions
1082 described in C can be decoded from the DF or DP curves was tested. In addition,

influences of external factors on the profiles of the DF or DP curves was assessed.

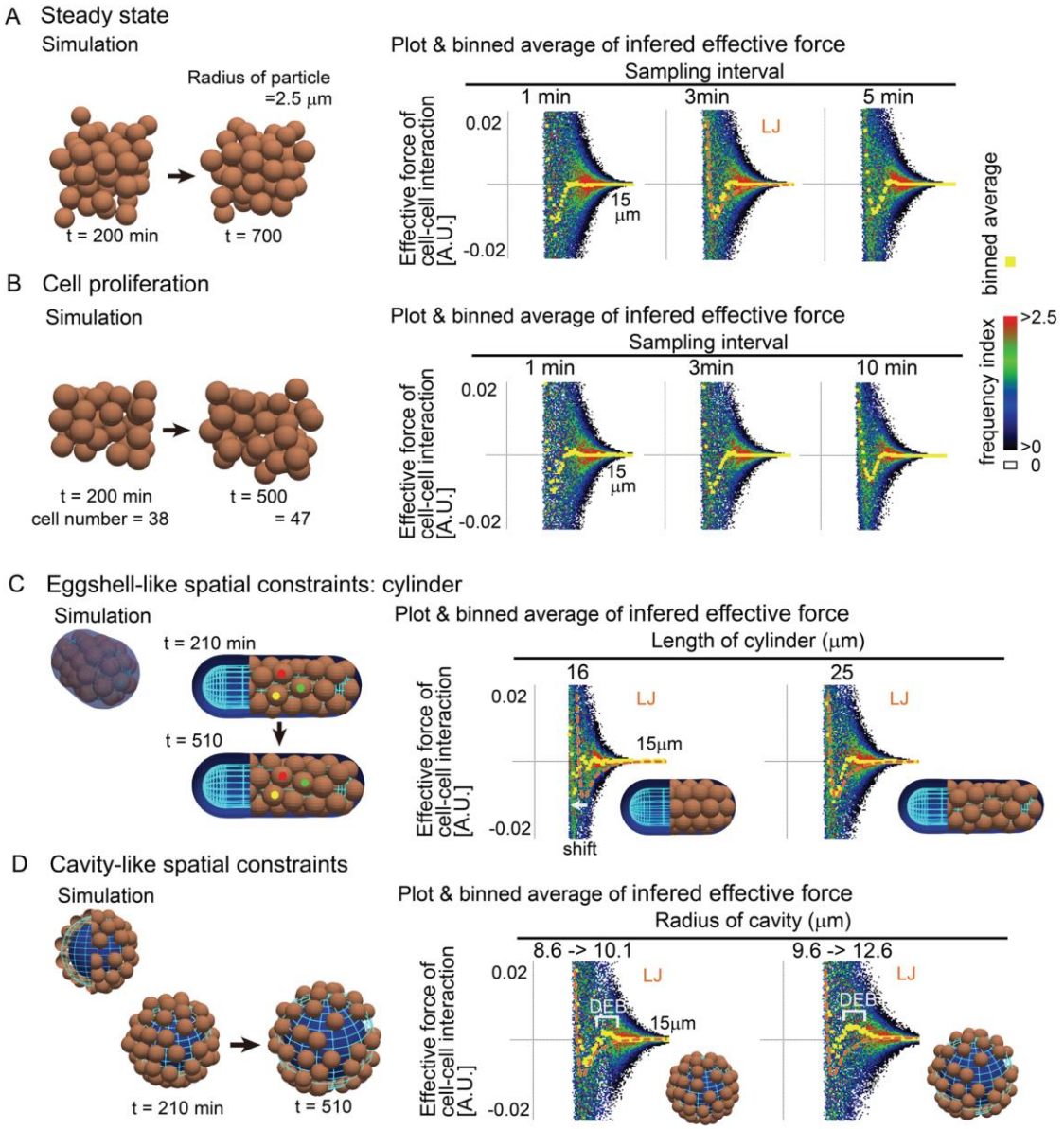

Figure 2: Validation of inference method using artificially generated data

Simulation data were used to validate our method for inferring effective forces of cell–cell interactions. The simulations were performed on the basis of a distance–force (DF) curve obtained from the Lenard-Jones potential (LJ). The simulation conditions contain

1092 “Steady state” (A), “Cell proliferation” (B), “Egg shell-like spatial constraints” (C), and
1093 “Cavity-like spatial constraints” (D). The left panels in A-D are snapshots of the
1094 simulations. The right panels in A-D are DF curves obtained from the inference. Effective
1095 forces of interactions for each pair of cells for each time frame were plotted against the
1096 distance of the cell–cell interactions. The graph space was divided into 64×64 square
1097 regions, and the frequencies of the data points plotted in each region were calculated. The
1098 mean value of the frequencies was calculated for each of the 64 columnar regions along
1099 the distance. Frequency index (FI) is defined so that the mean value of the frequencies is
1100 1, and a colored heat map was generated according to the FI. White corresponds to an FI
1101 of 0. Averaged values of the forces were calculated for 64 columnar regions along the
1102 distance, and are shown in yellow (binned average). Detailed procedures are described in
1103 SI (Section 4). In some graphs, the DF curves from the LJ potential are overlaid by orange
1104 broken lines (LJ). In A and B, simulation data with different sampling intervals were
1105 applied. In C, under the cylindrical constraint with a shorter length where particles are
1106 highly compressed, the DF curve was shifted leftward along the distance (white arrow).
1107 In D, on the expanding cavities, repulsive forces at distant regions were detected, which
1108 we called distant energy barriers (DEB). Related comprehensive analyses are shown in
1109 Figure S4 with simulation movies (Movies S8A-K). Detailed assumptions and conditions

of the simulations are described in SI, Section 7-4.

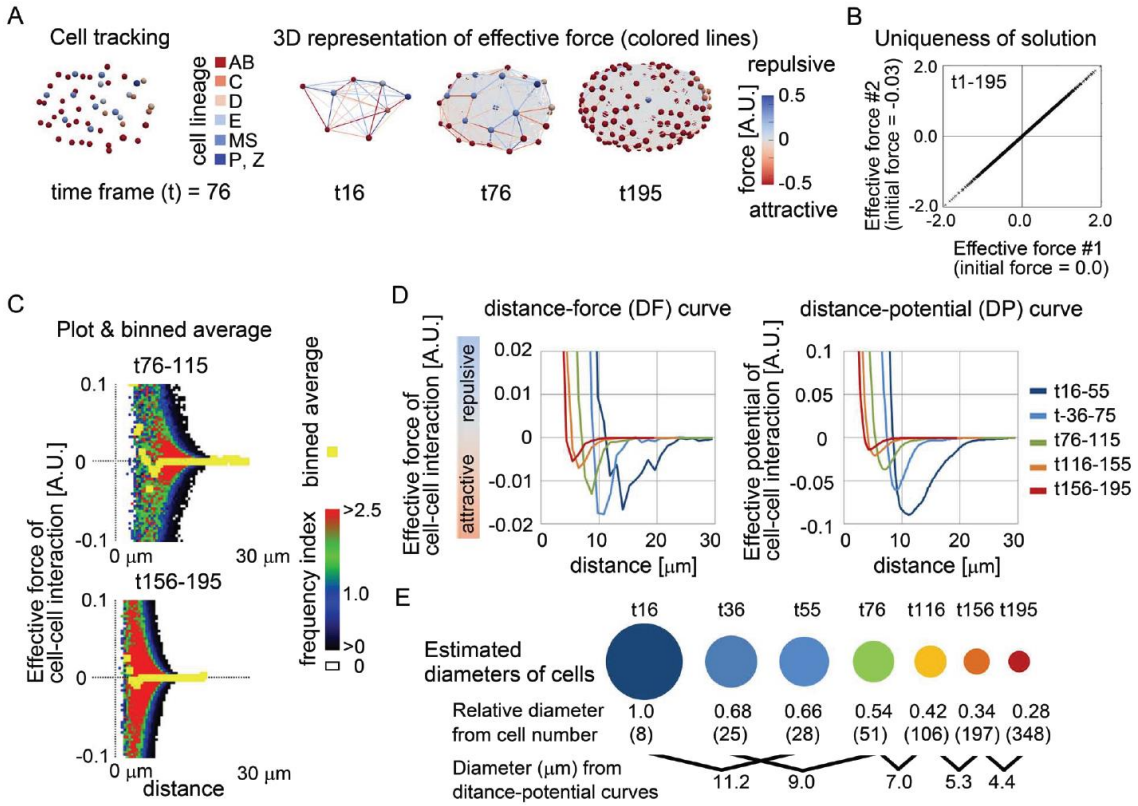

Figure 3: Inference of effective force of cell–cell interaction in *C.elegans* embryos

A. Snapshot of the nuclear positions in the *C.elegans* embryo (left panel) and snapshots with inferred effective forces (right three panels) were three-dimensionally visualized at the time frames as described (t16, t76, and t195); the interval between time frames is 1 min. The spheres correspond to cells whose colors represent cell lineages, including AB, C, D, E, MS, and P & Z. The lines represent cell–cell interactions; the colors indicate the values of the effective forces (red, attractive; blue, repulsive). Forces are depicted in arbitrary units (A.U.); 1 A.U. of the force can move a particle at 1μm/min as described in SI (Section 4-4). The nuclear tracking data were obtained from a previous report [32].

Related figures and movies are provided (Fig. S6A, B, Movies S3A and B). B. Uniqueness of solution of effective force inference was examined. The minimizations of Equation S6 were performed from different initial force values as described in the x- and y- axes, and the inferred values of each cell-cell interaction were plotted by crosses. The inferred values from the different initial force values were absolutely correlated. Values from all time frames (t1-195) were applied. C. The inferred effective forces of cell–cell interactions were plotted against the distance of cell–cell interactions in a manner similar to Figure 2. The graphs for time frame 76–115 and 156–195 are shown. Data at other time frames are provided in Figure S6C. D. Distance–force (DF) and distance–potential (DP) curves were estimated. The averaged values of the effective forces in (C) were smoothed over the distance, and the potentials were calculated by integrating the forces. Details are described in SI (Section 5-3). The curves for each time frame are shown. E. Mean diameters of cells at each time frame were estimated from cell numbers and the DP curves. Given that the volume of the embryos is constant (= Vol) during embryogenesis, the mean diameters were estimated from the cell numbers (N_c) at each time frame as follows: mean diameter = $\{Vol / (4/3\ \pi\ N_c)\}^{1/3}$. The diameters relative to that at time frame = 16 are shown with cell numbers (parentheses). The sizes of the circles reflect the diameters, whose colors roughly correspond to the colors in the graph in D. The diameters were also

estimated from the DP curves in D; the distances with minima of the DP curves roughly reflect the diameters (Fig. 1B and S2D).

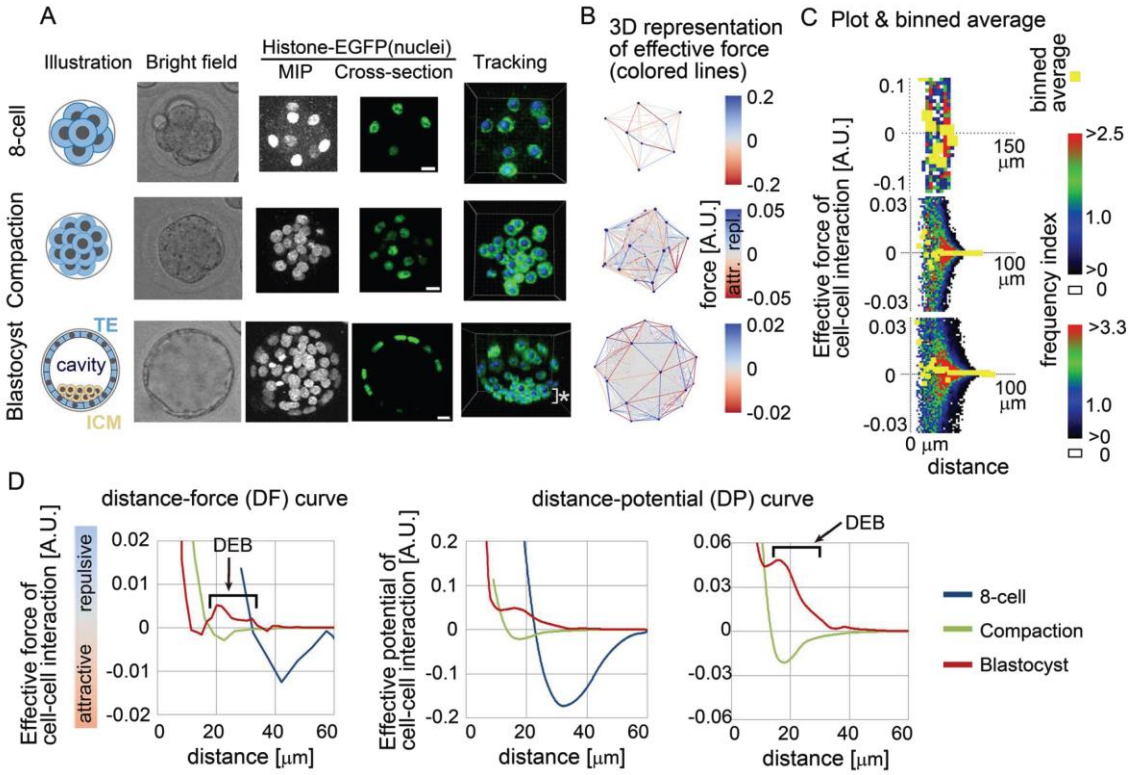

Figure 4: Inference of the effective force of cell–cell interaction in mouse pre-implantation embryos

A. Eight-cell, compaction, and blastocyst stages of mouse embryo are illustrated, and their confocal microscopic images are shown: bright field, maximum intensity projection (MIP) and cross-section of fluorescence of H2B-EGFP. Snapshots of nuclear tracking are also shown; blue spheres indicate the detected nuclei. In the illustration of the blastocyst, ICM and TE cells are depicted by orange and blue, respectively, and a cavity is also described. In the nuclear tracking image of the blastocyst, ICM cells are located around the bottom region of the image, as indicated by *. Scale bars = 15µm. Related movies are

1157 provided (Movie S4A–C). B. Snapshots of nuclear positions with inferred effective forces
1158 were visualized three-dimensionally for the three embryonic stages in a manner similar
1159 to Figure 3A. Blue spheres correspond to cells. The lines represent cell–cell interactions,
1160 and the colors indicate the values of the effective forces [red, attractive (attr.); blue,
1161 repulsive (repl.)]. Related movies are provided (Movie S4D-G). The uniqueness of the
1162 solutions was confirmed in Figure S10B. C. The inferred effective forces of cell–cell
1163 interactions were plotted against the distance of cell–cell interactions in a manner similar
1164 to Figure 2, except that the graph space of the 8-cell stage was divided into 32×32 square
1165 regions, and the averaged values were calculated for the 32 columnar regions. D.
1166 Distance–force (DF) and distance–potential (DP) curves were estimated from (C) in a
1167 manner similar to Figure 3D. A distant energy barrier (DEB) was detected, as indicated
1168 by arrows. Data from other embryos are provided in Figure S6D. The differences in DF
1169 and DP curves between ICM and TE cells and between the outer and inner cells in the
1170 compaction state were described in Figure S6. DP curves between adjacent cells are
1171 provided in Figure S8A-C. Directional differences of DP curves, which may correspond
1172 to cell polarity, are discussed in Figure S9 and S15D.

1173

1174

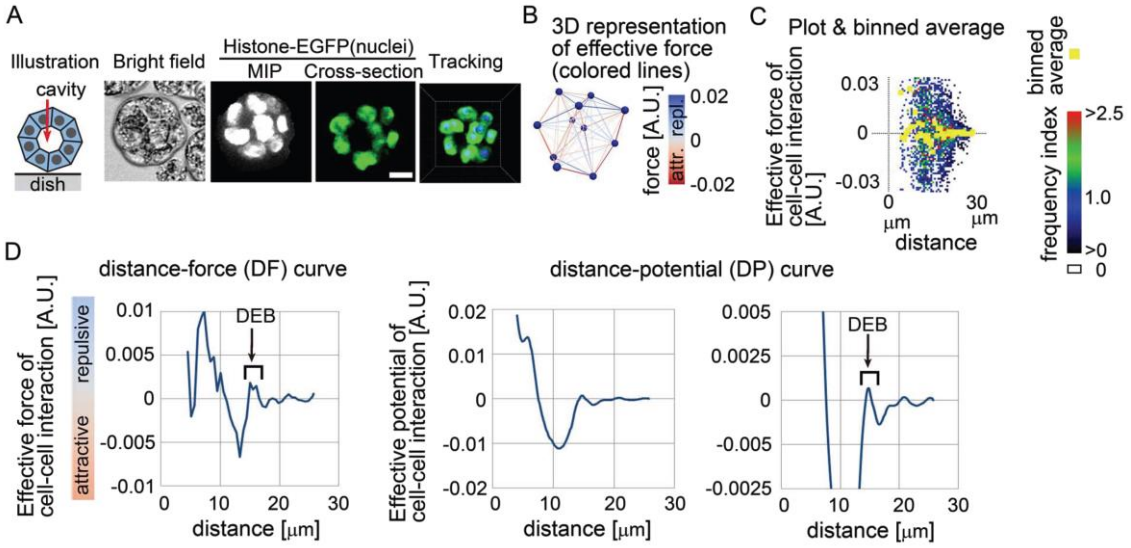

Figure 5: Inference of effective force of cell–cell interaction in cysts formed by MDCK cells

A. MDCK cysts formed under suspension conditions are illustrated, and confocal microscopic images are shown: bright field, maximum intensity projection (MIP) and cross-section of fluorescence of H2B-EGFP. A snapshot of nuclear tracking is also shown; blue spheres represent nuclei. Scale bars = 10μm. A related movie is provided (Movie S5A). B. A snapshot of the nuclear positions with inferred effective forces was three-dimensionally visualized in a manner similar to Figure 3A. The blue spheres correspond to cells. The lines represent cell–cell interactions and the colors indicate the values of the effective forces [red, attractive (attr.); blue, repulsive (repl.)]. A related movie is provided (Movie S5B). The uniqueness of the solutions was confirmed in Figure S10C. C. The

1188 inferred effective forces of cell–cell interaction were plotted against the distance of cell–
1189 cell interaction in a manner similar to Figure 3C. D. Distance–force and distance–
1190 potential curves were estimated from (C) in a manner similar to Figure 3D. DEB was
1191 detected as indicated by arrows. Data from other cysts are provided in Figure S6E. DP
1192 curves between adjacent cells are provided in Figure S8D.

1193

1194

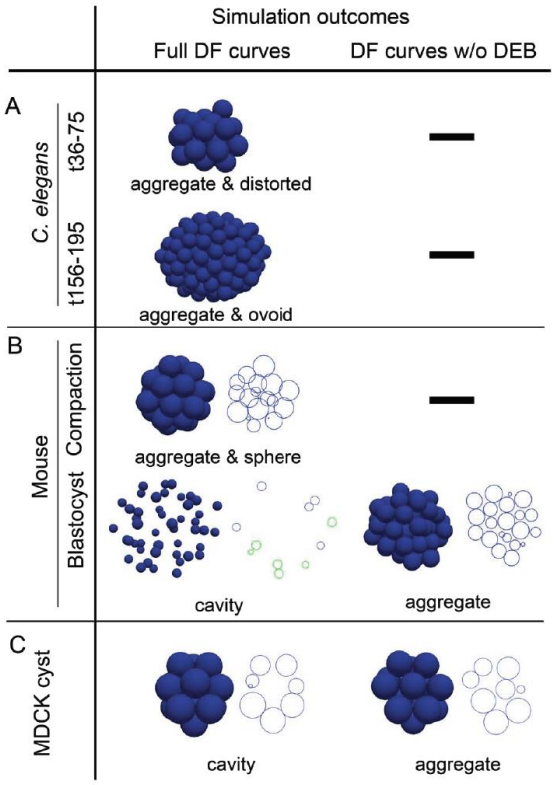

Figure 6: Outcomes of simulations based on inferred distance–force curves

Simulations results under the DF curves derived from *C. elegans* (A) and mouse embryos (B), and the MDCK cyst (C) are shown. Blue spheres correspond to cells. In the *C. elegans* embryos, the DF curves were derived from time frames 36–75 and 156–195 in Figure 3D. In the mouse embryos, the DF curves were derived from the compaction and blastocyst stages in Figure 4D. Cross-sections are also visualized. In the case of the mouse blastocyst, two parallel cross-sections (shown in blue and green) are merged. In the MDCK cyst, the DF curves are derived from Figure 5D. In the blastocyst and the MDCK cyst, the DF curves without DEB were also applied (w/o DEB). The diameters of the blue

spheres are set to be equivalent to the distance with the minimum potential (Fig. S2D). The initial configurations of the simulations are described in Figure S11, along with other simulation results.

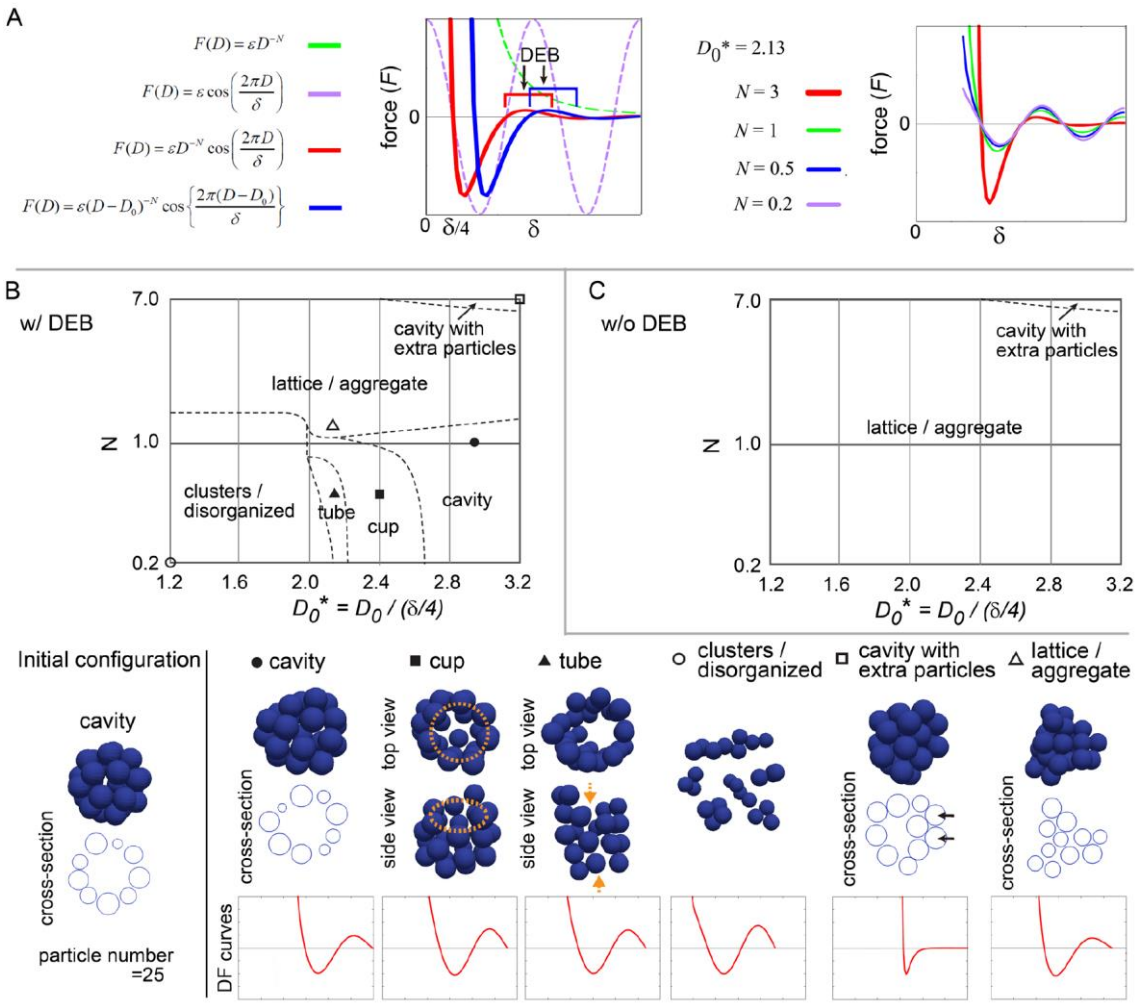

Figure 7: Modeling of distance–force curves and diagrams of simulation outcomes

A. DF curves were mathematically modeled using four parameters: N, D_0, δ, and ε. In the case of the DF curves without the cosine term, the curves ($F = \varepsilon\ (D - D_0)^{-N}$) are always >0 (repulsive) and gradually approach 0 as D increases (green broken line). Upon introduction of the cosine (purple broken line), the curves acquire regions with <0 (attractive) and DEB (red line). Upon introduction of D_0, the curves are translated along the distance (blue line). N affects the gradient of the curves and the height of DEB (right

panel). DF curves from $D = 0$ to D at the end of DEB (w/ DEB) or the curves from $D = 0$ to D before starting DEB (w/o DEB) were used in the following simulations. The physical meaning and interpretation of these parameters are described in SI, Section 6. B. Simulations were performed starting from an initial configuration, and the outcomes under various values of N and D^* are shown in the diagrams. A cavity-bearing structure was given as the initial configuration; the blue spheres correspond to cells, and a cross-section is visualized. According to the conditions, a cavity was maintained, whereas cups, tubes, etc. were generated. Some conditions on the diagram were designated by symbols (circle, square, and triangle), and their simulation results are visualized (blue spheres). Example profiles of the DF curves are shown. The diameters of the blue spheres are set to be 0.5× the distance with the minimum potential, which corresponds to the distance with $F = 0$ (arrows in the profiles of the DF curves, Fig. S2D). In the case of the cup, the mouth of the cup is marked by orange rings. In the case of the tube, the open ends of the tube are shown by orange arrows. In the case of the cavity with extra particles, the extra particles are shown by arrows. C. Simulation outcomes are shown on diagrams similar to B, except that the simulations were performed without DEBs. Other diagrams are provided in Figure S12.

1238

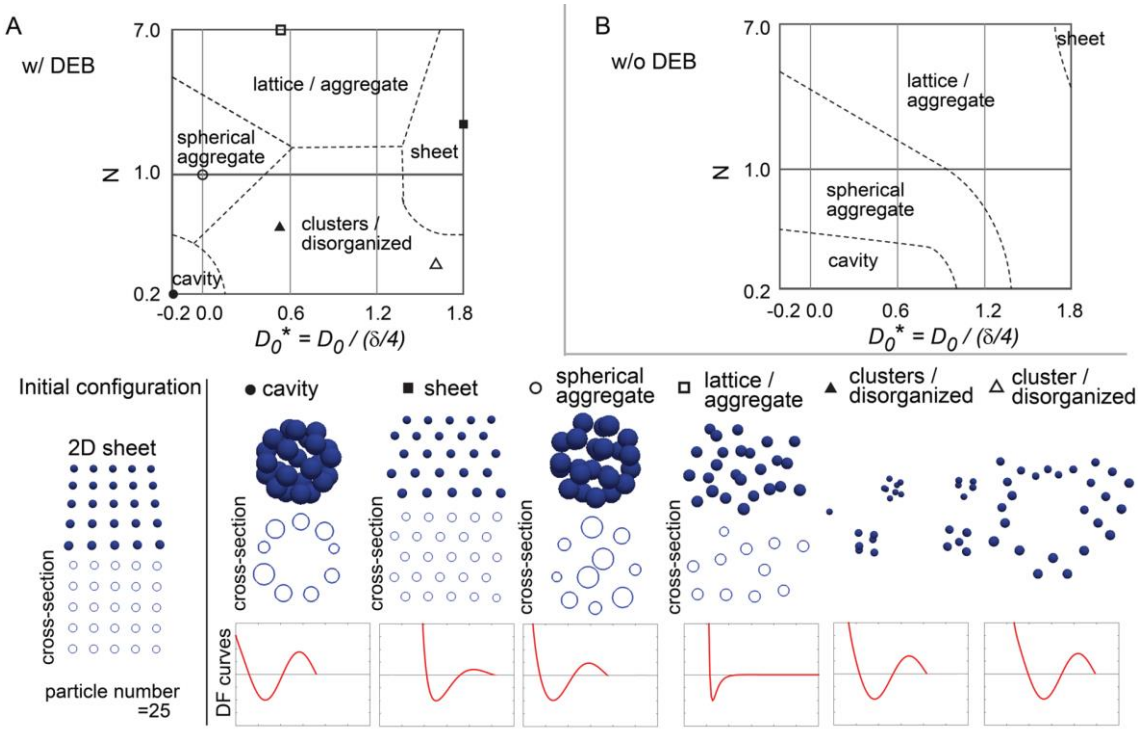

Figure 8: Simulation outcomes and their diagrams, based on distance–force curves; starting from 2D sheet

A. Simulations were performed from a two-dimensional (2D) sheet with slight positional fluctuations under various distance–force curves defined by Equation 3 (Fig. 7A), and a diagram of the outcomes is shown. The number of particles was set to 25. Cross-sections are also presented (blue circles). According to the conditions, the 2D sheet was maintained, whereas aggregates, cavity-bearing structures etc. were generated. The diameters of the blue spheres are set to be 0.2× the distance with the potential minimum.

B. Similar to A, except that the simulations were performed without distant energy

barriers (DEBs). 2D sheets were maintained, but the area in the diagram became significantly smaller than that in A. Thus, the maintenance of 2D sheet is enhanced by DEBs. In addition, cavities were generated without DEBs. Other diagrams are provided in Figure S12.

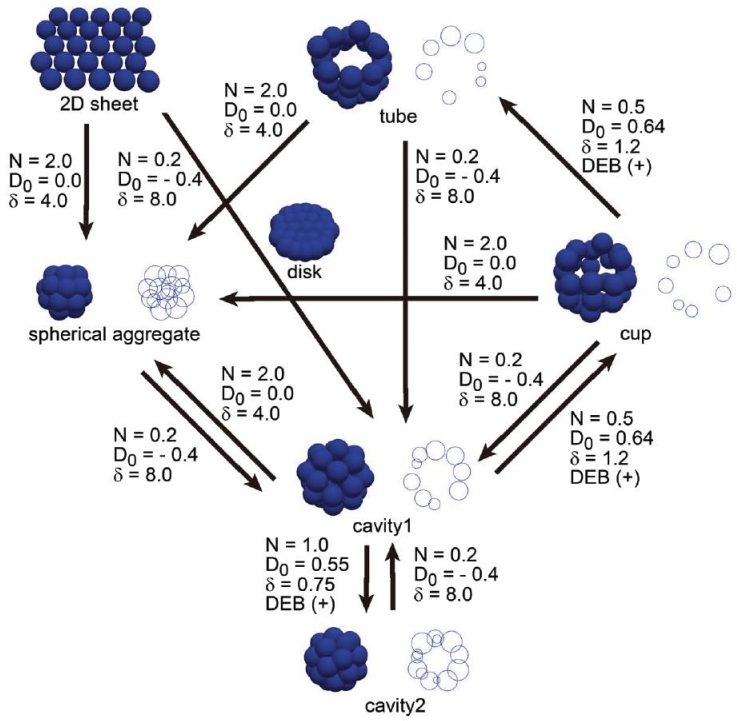

Figure 9: Morphological transitions achieved by distance–force curves

Possible morphological transitions that can be achieved by modulating the values of three variables: N, D_0, and δ in Figure 7. The values of the variables are presented. Conditions with DEB are indicated as DEB (+). The analysis focused on specific structures: cavity-bearing structures, cup, tube, spherical aggregate, two-dimensional sheet, and disk. The cup is a transition state from the cavity-bearing structure to the tube. The disk is also a transition state from the two-dimensional sheet to the cavity-bearing structure. A related movie is provided (Movie S6).